Ultrafast dynamics of skyrmion materials

Masterarbeit in Physik
von
Evgeniia Slivina
angefertigt im
II. Physikalisches Institut,
Universität zu Köln

vorgelegt der
Mathematisch-Naturwissenschaftlichen Fakultät
der
Rheinischen Friedrich-Wilhelms-Universität
Bonn

November 2016

I hereby declare that this thesis was formulated by myself and that no sources or tools other than those cited were used.

Bonn, ...
Date Signature

1. Gutachter:	Prof. Dr. Paul H.M. van Loosdrecht
2. Gutachterin:	Prof. Dr. Corinna Kollath

Contents

Abstract

During the course of this thesis, the ultrafast dynamics of skyrmion materials was studied. The main focus of the work was GaV_4S_8, for which the first evidence of skyrmion lattice was obtained only recently. Moreover, this material undergoes a structural phase transition, the so-called Jahn-Teller distortion, so spontaneous Raman and differential reflectivity measurements were conducted in order to see how the phonon spectra changes with change in symmetry. We attempted to determine which of the observed modes are JT-active. In order to study the magnetization dynamics of GaV_4S_8, the TR-MOKE double-modulation technique was used, which was the first time the ultrafast optical spectroscopy was used to probe magnetization dynamics of this material . The TR-MOKE measurements were also conducted for Cu_2OSeO_3 in order to see if we can observe the magnetization dynamics in Kerr geometry.

1 Introduction

While studying hadrons in nuclear physics in 1960s, Tony Skyrme showed that certain particles are topologically protected [1]. These particles were named skyrmions and for a long time were considered unusual non-equilibrium entities which cannot be easily observed. This assumption was proven incorrect with the discovery of a skyrmion lattice in the chiral phase of the transition-metal compound MnSi using small-angle neutron scattering (SANS) [2]. Moreover, it was predicted in various theoretical works [3–7] that topologically protected quasiparticles can be observed in solid state materials such as chiral magnets in the form of stable spin vortices - magnetic skyrmions (Fig. 1).

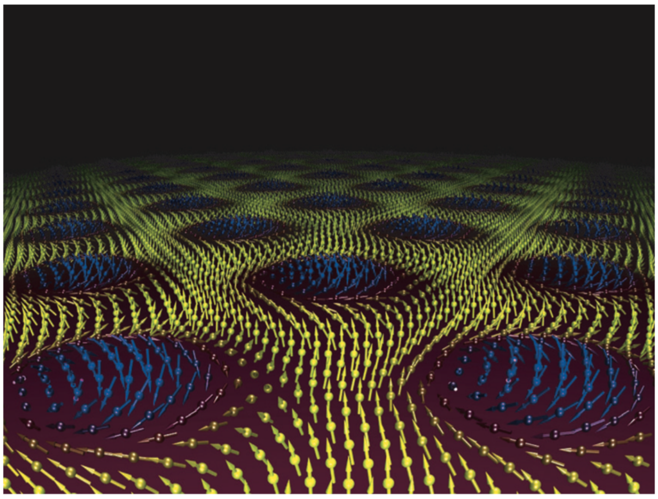

Figure 1: Schematic drawing of a skyrmion lattice [8].

The resemblance of skyrmions to magnetic bubbles, which were considered to be possible nanostructures for data storage applications [9], implies, for the former, an eventual technical applications in spintronics [10]. The reduced critical current density and magnetic fields for skyrmion materials and the stability of the skyrmion lattice may allow for low energy operation in future memory devices [11]. Skyrmions can also be represented as circulating dissipationless spin currents. This property gives rise to the possible applications of skyrmionic crystals in the branch of spintronics focused on the manipulation of a pure spin currents without charge transfer [12]. Such currents can bypass the constraints of conventional electronics and give rise to low-power and high-bandwidth information transfer [13].

Topologically protected spin-vortices were first observed in metallic compounds with cubic structure such as MnSi, $\mathrm{Fe}_{1\text{-x}}\mathrm{Co}_{\mathrm{x}}\mathrm{Si}$ and FeGe [2, 14–16]. Subsequently, observations of skyrmions were reported in various bulk and thin film systems. One example of such a compound is the chiral lattice magnet Cu_2OSeO_3 [17], one of the materials central to this work. The presence of a skyrmion lattice was experimentally shown primarily for materials with non-centrosymmetric chiral structure. In this type of crystal, topologically protected spin vortices are formed by Bloch-type domain walls, which leads to the formation of vortex-like skyrmions. In the case of Bloch domain walls, the spins rotate in the plane parallel to the domain boundary. Hence, in Bloch skyrmions, the spins rotate in tangential planes when moving from the center of the vortex to the periphery. However, in polar magnets with a C_{nv} crystal symmetry, another type of skyrmions is formed - Néel skyrmions [3, 4, 18]. This type of skyrmion is induced by Néel domain walls, where the spins rotate in a plane perpendicular to the domain boundary, leading to the formation of a structure with spins rotating in the radial planes from the center to the periphery (Fig. 2). In this work, the magnetic semiconductor GaV_4S_8 was investigated as an example of a material supporting Néel skyrmions.

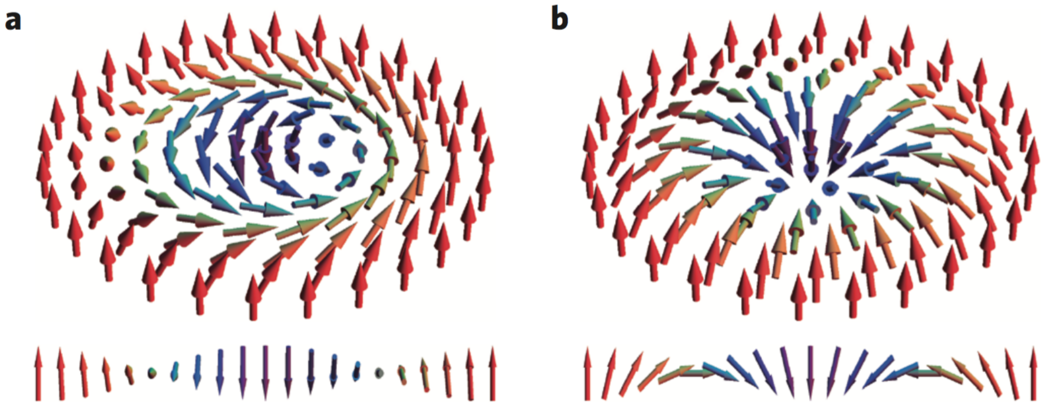

Figure 2: Bloch (a) and Néel (b) type skyrmions [19].

In recent years, numerous techniques were used in order to observe skyrmions in magnets, including SANS (which was mentioned above as the first experimental evidence of a chiral magnet hosting skyrmion phase), LTEM (Lorentz transmission electron microscopy) [15], MFM (magnetic force microscopy) [20], and spin-resolved scanning tunneling microscopy [21, 22]. In order to study the dynamics of skyrmions it is also possible to use optical techniques. Previously, single skyrmions have been created by ultrafast laser excitation in thin ferromagnetic films [23, 24]. In the same way, ultrafast optical spectroscopy is a promising tool for the investigation of Cu_2OSeO_3 and GaV_4S_8, because it allows for the manipulation of the magnetic order. It provides the opportunity to trigger and subsequently detect electronic excitations, and hence, the magnetization dynamics of the materials on small time scales. Tokura *et al.* used the inverse-Faraday effect to excite the skyrmion phase in Cu_2OSeO_3 and detected the resultant spin dynamics via time-resolved magneto optics [25]. We extended upon these findings by employing the time-resolved magneto-optical Kerr effect (TR-MOKE). Additionally, we studied vibrational properties of GaV_4S_8 to probe the Jahn-Teller distortion via measuring spontaneous Raman spectra and differential reflectivity of a sample.

2 Skyrmions

2.1 Skyrmion spin structures and their properties

Originally proposed in nuclear physics to describe certain particles as localized states [1], skyrmions turned out to be a very interesting concept for condensed matter physics. In recent years, skyrmions have been actively studied in the field of solid state magnetism. A magnetic skyrmion is a topological particle in real space, which is composed of spins pointing in all directions wrapping a sphere and resembles a hedgehog. In 2D space a hedgehog configuration can be projected on a plane as a skyrmion (Fig. 3).

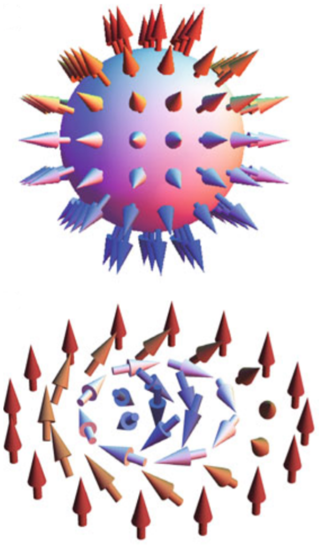

Figure 3: Schematic image of the original hedgehog-like skyrmion proposed by Skyrme (top) and a projection of it on a two-dimensional plane (bottom) [26].

The number of wrappings of the spins around a sphere is called *winding number*. This number is a topological invariant, thus the skyrmions have topologically protected stability. The winding number in the case of a projected skyrmion is given by [26]

$$\mathscr{G} = \int d^2r \left(\frac{\partial \hat{\mathbf{n}}}{\partial x} \times \frac{\partial \hat{\mathbf{n}}}{\partial y} \right) \cdot \hat{\mathbf{n}}, \tag{2.1}$$

where $\hat{\mathbf{n}} = \mathbf{M}/\left|\mathbf{M}\right|$ is the unit vector pointing in the direction of magnetization. For a single skyrmion, the value of $\mathscr{G}$ is given by $4\pi Q$, where $Q = \pm 1$ is the skyrmion number. The sign of Q corresponds to the spin state at the skyrmion core: $Q = 1$ for spin up and $Q = -1$ for spin down. The possible types of skyrmion structure can be described by vorticity m ($+1$ for a skyrmion and -1 for an anti-skyrmion) and helicity γ, as shown in Figure 4. Dependence of m and γ on the energy required for the formation of the skyrmions varies for different mechanisms of skyrmion generation [11].

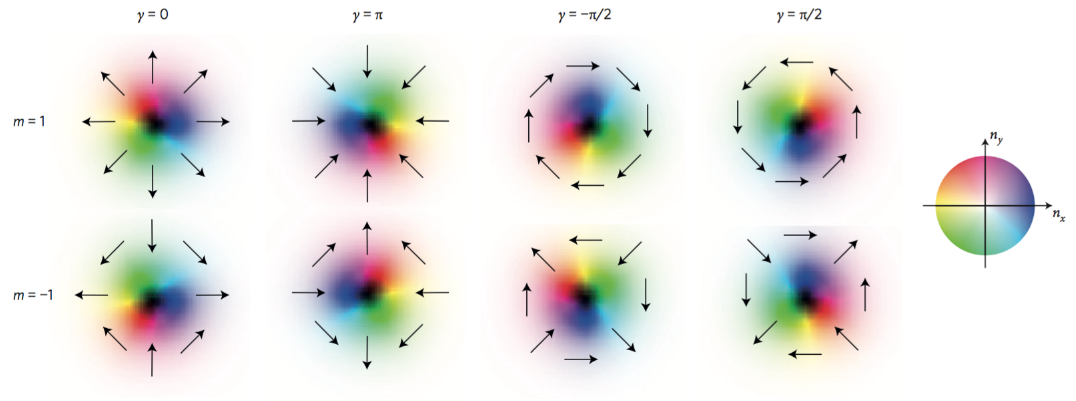

Figure 4: Skyrmion structures with different values of vorticity m and helicity γ. The arrows point in the direction of in-plane spin components and the brightness indicates the direction of spin components normal to the plane (white- up direction, black- down direction) [11].

Skyrmion spin structures can be formed and stabilized by a variety of mechanisms which can contribute simultaneously. Long-range magnetic dipolar interactions dominate in magnetic thin films with perpendicular easy-axis anisotropy, where the dipolar interaction prefers an in-plane magnetization while the anisotropy prefers out-of plane magnetization. These interactions compete with each other, leading to the formation of a periodic array of magnetic bubbles or skyrmions, with sizes ranging from 100 nm to 1 μm depending upon the applied magnetic field oriented perpendicular to the film [9, 27–29]. For the formation of atomic-sized skyrmion structures (on the order of the lattice constant ($\backsim$1nm)), the dominant mechanisms are frustrated exchange interactions [30] and four-spin exchange interactions [22]. In non-centrosymmetric magnets, the formation of a skyrmion lattice is caused by competition between the Dzyaloshinskii-Moriya (DM) and ferromagnetic exchange interactions. In this case, the size of a single skyrmion is typically 5-100 nm. When skyrmion spin structures are generated by DM or long-ranged magnetic dipolar interactions, skyrmions are larger than a lattice constant allowing for use of the continuum approximation. These large-scale skyrmions have many internal degrees of freedom and are highly mobile [11]. The materials studied in this work are non-centrosymmetric magnets, hence the DM interaction is responsible for the formation of the skyrmion lattice. This case is considered in more detail in the next section.

2.2 Skyrmions in non-centrosymmetric magnets

In magnets without spatial inversion symmetry, the Dzyaloshinskii-Moriya (DM) interaction (which originates from the relativistic spin-orbit coupling) becomes finite [31, 32]. In a continuum spin model, the DM interaction is given by:

$$\mathscr{H}_{\mathrm{DM}} \propto \int d\mathbf{r}\mathbf{M} \cdot (\nabla \times \mathbf{M}) \,, \tag{2.2}$$

where $\mathbf{M}$ is the classical magnetization vector. The DM interaction competes with the ferromagnetic exchange interaction ($J > 0$) which can be written as:

$$\mathscr{H}_{\mathrm{ex}} \propto \int d\mathbf{r} \left(\nabla \mathbf{M}\right)^2 . \tag{2.3}$$

As a result of this competition, a helical spin order with a uniform turn angle is realized in the absence of an external magnetic field. In 1980, Bak and Jensen proposed the continuum spin model to describe the magnetism in MnSi as a prototypical chiral magnet [33]. In their model they considered the following Hamiltonian:

$$\mathscr{H} = \mathscr{H}_{\mathrm{ex}} + \mathscr{H}_{\mathrm{DM}} + \mathscr{H}_{\mathrm{Zeeman}} + \textit{magn. anisotropies}, \tag{2.4}$$

where:

$$\mathscr{H}_{\mathrm{ex}} = \int d^3r \frac{J}{2a} \left(\nabla \mathbf{M}\right)^2, \tag{2.5}$$

$$\mathscr{H}_{\mathrm{DM}} = \int d^3r \frac{D}{a^2} \mathbf{M} \cdot (\nabla \times \mathbf{M}), \tag{2.6}$$

$$\mathscr{H}_{\mathrm{Zeeman}} = -\int d^3r \frac{1}{a^3} \mathbf{B} \cdot \mathbf{M}, \tag{2.7}$$

$$\textit{magn. anisotropies} = \int d^3r \frac{A_1}{a^3} \left(M_x^4 + M_y^4 + M_z^4\right)$$

$$-\int d^3r \frac{A_2}{2a} \left((\nabla_x M_x)^2 + (\nabla_y M_y)^2 + (\nabla_z M_z)^2 \right). \tag{2.8}$$

Equation (2.7) represents Zeeman coupling to an external magnetic field $\mathbf{B}$ and equation (2.8) describes the magnetic anisotropies allowed by a cubic crystal symmetry. As long as the small values of the constants A_1 and A_2 are considered, this term of the Hamiltonian doesn't play a major role in the continuum spin model. The lattice constant is given by a. The continuum approximation is justified when D/J is small and this ratio determines the period of a skyrmion lattice. Starting from the continuum model given by equation (2.4), one can obtain a classical Heisenberg model on the cubic lattice by dividing the space into cubic meshes.

In order to study the stability of a skyrmion phase in the continuum spin model, one can write the Ginzburg-Landau free energy functional near the critical temperature T_c . Ginzburg-Landau theory gives a continuum characterization of the various phase transitions. This phenomenological theory is based on the existence of an order parameter which is non-zero in the ordered phase below T_c and becomes zero above T_c. Close to the phase transition the order parameter is small and the energy functional can be expanded as a power series around the order parameter [34]. The Ginzburg-Landau free energy functional for a chiral lattice magnet can be written as (2.9) [2]

$$F[\mathbf{M}] = \int d^3r \left[r_0\mathbf{M}^2 + J\left(\nabla\mathbf{M}\right)^2 + 2D\mathbf{M}\cdot(\nabla\times\mathbf{M}) + U\mathbf{M}^4 - \mathbf{B}\cdot\mathbf{M}\right]. \tag{2.9}$$

The first four terms of the equation (2.9) describe different interactions: J describes ferromagnetic exchange, D the DM interaction, and U the interaction between different modes. The last term describes Zeeman coupling. In our case the order parameter is the local magnetization $\mathbf{M}\left(\boldsymbol{r}\right)$. The state of the system and the value of the order parameter are determined by the condition of free energy minimization. The dimensionless (Gibbs) free energy G as a function of the applied magnetic field and temperature is given by equation

$$Z = exp(-G) = \int \mathscr{D}\mathbf{M}e^{-F[\mathbf{M}]}, \tag{2.10}$$

where Z is the partition function and $\mathscr{D}\mathbf{M}$ means integration over all possible configurations of $\mathbf{M}$. One can calculate free energy G using the mean-field approximation

$$G \backsim minF[\mathbf{M}] = F[\mathbf{M_0}], \tag{2.11}$$

where $\mathbf{M_0}$ is the minimum of the free energy functional F. In the mean-field approach one looks only at the stationary points of F, neglecting any fluctuations around these points. However, in order to reproduce the skyrmion phase it is necessary to take into account thermal fluctuations around the mean field value $\mathbf{M_0}$ and add a correction term to equation (2.11) [26]. Thus, the free energy is given by

$$G \approx F[\mathbf{M_0}] + \frac{1}{2}log\left[det\left(\frac{\delta^2F}{\delta\mathbf{M}\delta\mathbf{M}}\right)_{\mathbf{M}=\mathbf{M_0}}\right]. \tag{2.12}$$

In close proximity to T_c, the contribution from order parameter fluctuations is comparable to its mean-field value, and equation (2.12) becomes invalid.

2.3 Magnetic phases and spin dynamics of the skyrmion materials

The first experimental observation of a skyrmion lattice was made in the chiral non-centrosymmetric magnet MnSi in 2009 by means of SANS [2]. Since then, they have been observed in many other compounds as well. Besides MnSi, metallic materials with cubic structure, such as $Fe_{1-x}Co_xSi$ [14] and FeGe [16], were identified as skyrmion systems. Moreover, the presence of a skyrmion phase was experimentally observed in thin films (one-atomic-layer-thick Fe film on Ir(111) [22]) and centrosymmetric magnets (hexaferrite $Ba(Fe_{1-x-0.05}Sc_xMg_{0.05})_{12}O_9$ [35]). The insulating chiral lattice magnet Cu_2OSeO_3 is another example of a non-centrosymmetric material hosting a skyrmion phase. Since this compound is studied in the current work, the possible phases of a skyrmionic material are discussed using Cu_2OSeO_3 as an example.

The experimental magnetic phase diagram for Cu_2OSeO_3 obtained via Faraday rotation measurements is given in Figure 5. It shows ferrimagnetic and paramagnetic phases and three chiral phases – the helical, conical, and skyrmion (SkL) phase. The chiral magnetic phases will be considered in more detail later in this section.

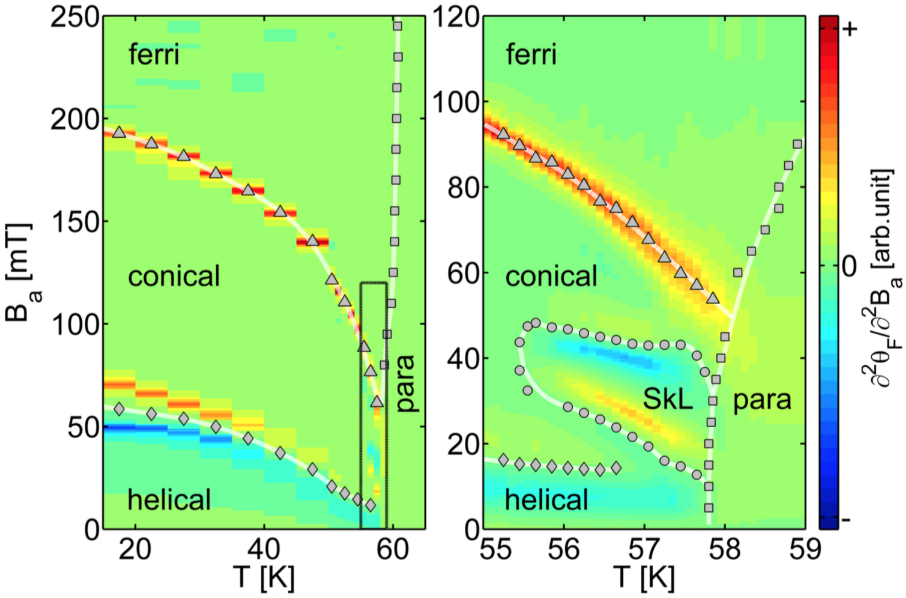

Figure 5: The magnetic phase diagram of Cu_2OSeO_3 obtained from a Faraday rotation. B_a is the applied magnetic field along (111) direction. The color mapping indicates the second derivative of Faraday rotation θ_F [36].

Helical phase: At zero applied magnetic field $\boldsymbol{B_a}$ and below the critical temperature T_c, Cu_2OSeO_3 exhibits helical magnetic order. In this phase, the magnetization rotates around an axis of the propagation vector $\boldsymbol{q}$ of the helix (Figure 6). The local magnetic moment $\mathbf{M}$ is perpendicular to $\boldsymbol{q}$.

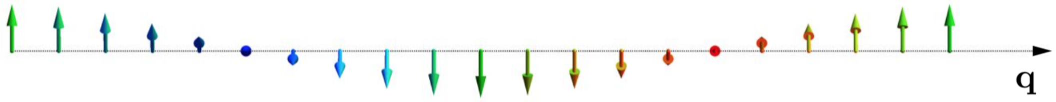

Figure 6: Twisting of the magnetization around an axis of the propagation vector $\boldsymbol{q}$ in helical phase [37].

The period of the helix λ_h equals to $2\pi/\left|\boldsymbol{q}\right|$, and can be determined from the competition of the ferromagnetic and Dzyaloshinskii-Moriya interactions, which is generally much larger than the lattice constant. The propagation direction of the helix $\hat{\mathbf{q}} = \mathbf{q}/\left|\mathbf{q}\right|$ is the result of the very weak magnetic anisotropies [38].

Conical phase: Increasing the magnetic field value above a critical field $B_{c1} < B_a$ and keeping the temperature below T_c leads to alignment of the multi-domain structure to the applied magnetic field. At a critical magnetic field value $B_{c2} > B_a$ the Dzyaloshinskii-Moriya interaction can be completely neglected and the transition to ferrimagnetic phase occurs. The intermediate region with $B_{c1} < B_a < B_{c2}$ corresponds to the so-called conical magnetic phase. The propagation vector $\boldsymbol{q}$ aligns along the direction of the applied magnetic field $\boldsymbol{B_a}$, and the local magnetization is no longer perpendicular to the vector $\boldsymbol{q}$, instead tilting in the direction of the magnetic field which leads to a uniform magnetization (see Figure 7).

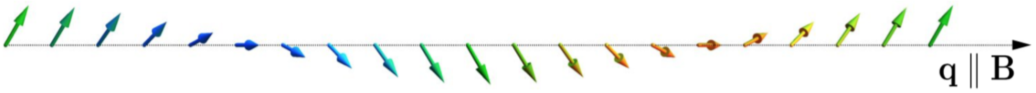

Figure 7: Alignment of the propagation vector $\boldsymbol{q}$ along the direction of the applied magnetic field [37].

A representation of the spin dynamics for the conical phase is depicted in Figure 8. In this case the spins, which are slightly tilted in the direction of magnetic field and propagation vector, evolve around the cones.

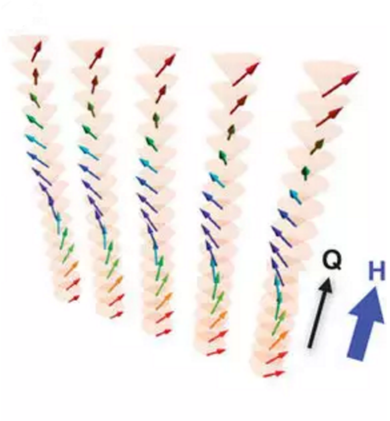

Figure 8: Spin dynamics of the conical phase, the colors represent the directions of the in-plane components (perpendicular to the propagation vector) in the conical structure [39].

Skyrmion phase: For finite applied magnetic field values $B_{c1} < B_a < B_{c2}$ in a small temperature region of the magnetic phase diagram close to T_c, a first order phase transition separates the skyrmion phase from the surrounding conical phase. The new ground state of the system is a two-dimensional hexagonal skyrmion lattice oriented perpendicular to the applied magnetic field. The lattice constant is given by $a_{SkL} = 2\lambda_h/\sqrt{3}$. The skyrmion lattice decouples from the atomic crystal lattice, such that the plane of the skyrmion lattice orients perpendicular to the applied magnetic field $\boldsymbol{B_a}$ independently of the underlying atomic orientation. The schematic image of the skyrmion lattice is given in Figure 9.

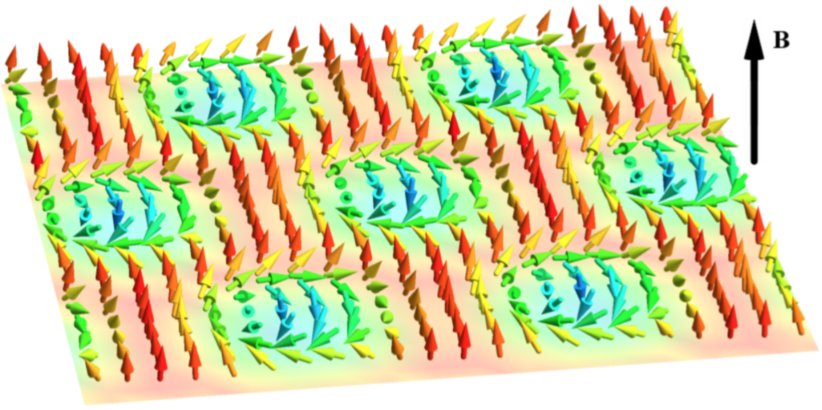

Figure 9: The two-dimensional skyrmion hexagonal lattice formed in the SkL phase [37].

Spin dynamics of a skyrmion crystal: The goal of this work is to study magnetization dynamics of the chiral magnet Cu_2OSeO_3 and the polar magnet GaV_4S.

Thus, one has to consider the response of the system to oscillating magnetic and electric fields H^{ω} and E^{ω}. Recently, the spin dynamics has been detected not only in the frequency domain but also in the time domain using pump–probe techniques[25]. For the skyrmion lattice spin state, theoretical studies have predicted several magnetic resonance modes characterized by different selection rules [40]. For an in-plane magnetic field, clockwise (CW) or counterclockwise (CCW) skyrmion rotational modes are expected. For an out-of-plane magnetic field, one expects to detect a breathing mode, which shrinks and expands in the plane perpendicular to the direction of magnetization **M**. Schematic drawings of the CW and CCW rotational modes and the breathing mode are given in Figure 10.

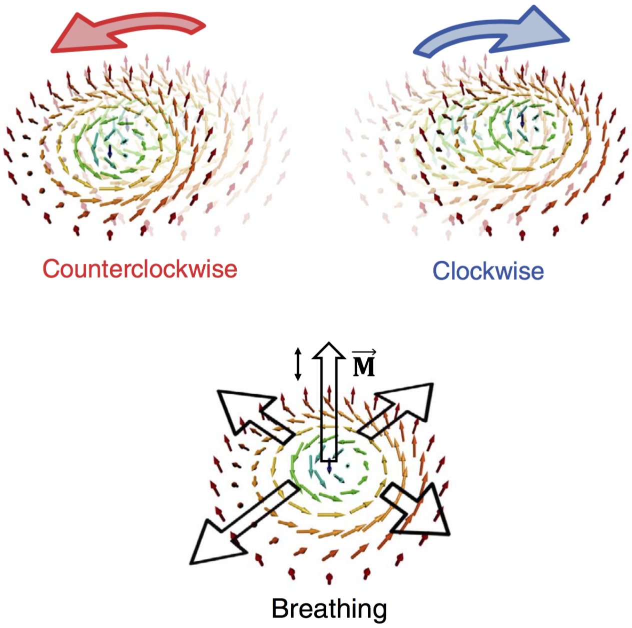

Figure 10: CW and CCW rotational modes of the skyrmion phase (in-plane magnetic field) and breathing mode (out-of-plane magnetic field) (adapted from [39]).

3 Bloch and Néel-type skyrmion lattice

Different kinds of skyrmion structures can be generated, depending on the type of domain walls. When ferromagnetic domains with ±**M** magnetizations are separated by a domain wall parallel to the **M** axis (180° domain wall), two main types of spin textures can emerge in the domain wall region. In cases where the magnetic moments show a screw-like continuous rotation within a plane parallel to the domain wall, the wall is called a "Bloch wall". This type of domain wall leads to formation of *Bloch skyrmions*. However, magnetic anisotropy can stabilize the cycloidal continuous rotation of magnetic moments within a plane normal to the domain wall. This type is called a "Néel wall" supporting *Néel skyrmions* are generated. The schematic drawings for both types of domain walls are given if Figure 11.

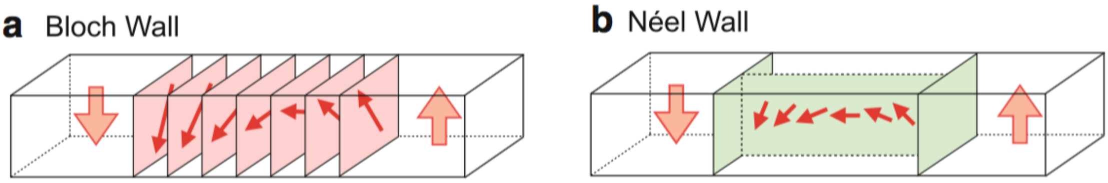

Figure 11: Bloch and Néel domain walls [26].

3.1 Cu_2OSeO_3

In Cu_2OSeO_3, Bloch skyrmions are generated by competition between the DM interaction and ferromagnetic exchange. This compound has a chiral and cubic structure similar to MgSi. Its crystal structure is given in Figure 12. Cu_2OSeO_3 is ferromagnetic with a Curie temperature around 60 K. At room temperature, it has the cubic space-group $P2_13$ which allows piezoelectricity but not a spontaneous polarization [41]. Below the critical temperature, the crystal structure of Cu_2OSeO_3 remains cubic but the magnetic ordering lowers the symmetry to space-group $R3$. Cu_2OSeO_3 lacks inversion symmetry.

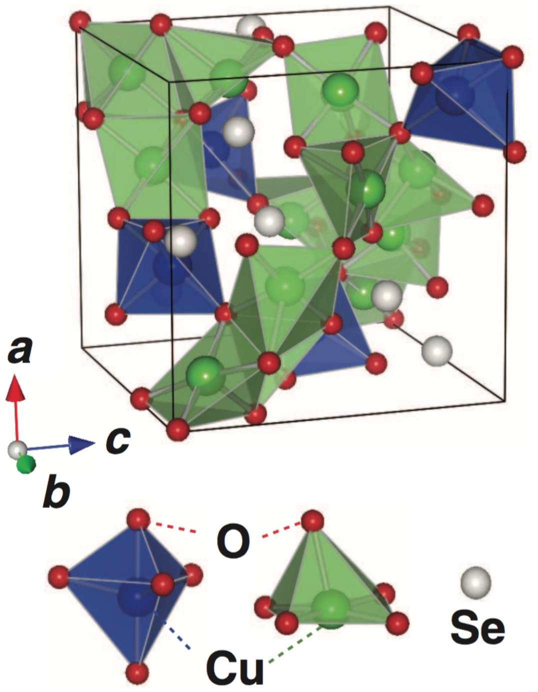

Figure 12: The crystal structure of Cu_2OSeO_3 [17].

The unit cell of Cu_2OSeO_3 contains 16 Cu^{2+} ions which form two non-equivalent copper sites with different oxygen ligand configuration (Cu_1 and Cu_2 sites). The local environment can be approximated by a trigonal bipyramid and square pyramid for Cu_1 and Cu_2 ions, respectively. The ratio of Cu_1 to Cu_2 sites in the unit cell is 1:3. Ferromagnetic exchange interactions between the neighboring sites are described by the Heisenberg Hamiltonian given by equation (2.5).

In the unit cell, four spin clusters are formed (Figure 13). The electron configuration of the Cu atom reduces from $[\mathrm{Ar}]3d^{10}4s^1$ to $[\mathrm{Ar}]3d^9$ for a Cu^{2+} ion which leads to absence of an electron from the outer shell. In each cluster there are three spins up ($s = \frac{1}{2}$) and one spin down ($s = -\frac{1}{2}$). The total spin of the spin cluster is then $S = 1$. The coupling constants J correspond to the exchange interaction of spins within separate copper tetrahedra and between different tetrahedra. Due to the complex crystal structure of Cu_2OSeO_3, there are five different coupling constants.

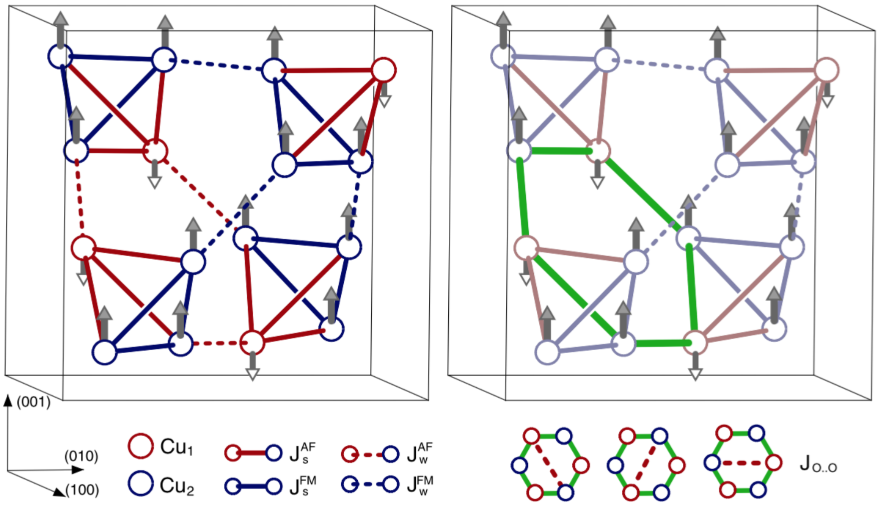

Figure 13: The unit cell of Cu_2OSeO_3 [42].

The ”strong” coupling constants are J_s^{AF} and J_s^{FM}. These constants describe spin exchange interaction within the clusters. The coupling constants J_w^{AF}, J_w^{FM}, and $J_\mathrm{o...o}^{AF}$ (the last one is a long-range coupling constant) characterize ”weak” coupling corresponding to spin exchange interaction between different clusters. The AF and FM correspond to the antiferromagnetic and ferromagnetic spin exchange interactions, respectively.

Since Cu_2OSeO_3 is chiral and lacks inversion symmetry, there is also an antisymmetric Dzyaloshinskii-Moriya (DM) exchange interaction, that competes with the stronger Heisenberg interaction. The coupling constant of the DM interaction is associated with the bond between the different spins. The DM interaction term is zero when the spins are perfectly aligned (cross product in equation (2.6) is zero). The competition between the Heisenberg and DM exchange interactions results in long-range helimagnetic order with the period of the helices proportional to $\frac{\mathrm{D}}{\mathrm{J}}$.

3.2 GaV$_4$S$_8$

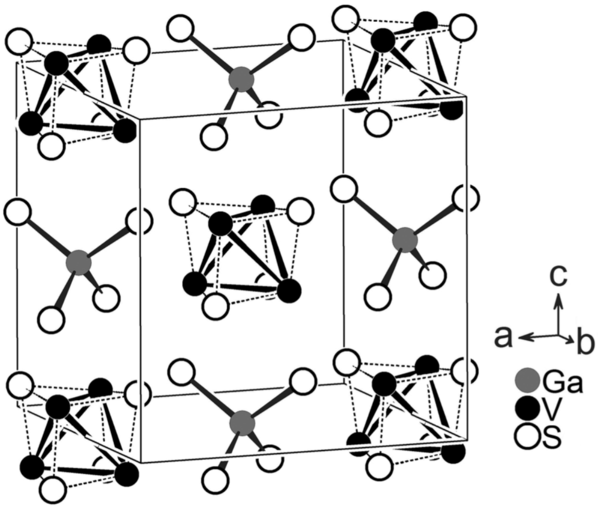

Figure 14: The crystal structure of GaV$_4$S$_8$ [43].

The polar magnet GaV$_4$S$_8$ also hosts a skyrmion phase, but the skyrmions generated in this material are of the Néel type. The crystal structure of GaV$_4$S$_8$is given in Figure 14. This is a Mott insulator having a lacunar spinel structure with a general formulation AB_4S_8. In this structure type, there are $(B_4X_4)^{n+}$ cubic and $(AX_4)^{n-}$ tetrahedral cluster ions, which are weakly coupled in an NaCl configuration [44]. For GaV$_4$S$_8$, these clusters are $(V_4S_4)^{5+}$ and $(GaS)^{5-}$, respectively. The difference from a cubic spinel structure AB_2S_4 is that one-half of the tetrahedral A sites remain empty, which leads to a reduction of symmetry from the space group $Fd\bar{3}m$ to $F\bar{4}3m$. Since the distances between the four vanadium atoms in the $(V_4S_4)^{5+}$ clusters are significantly shorter than between vanadium atoms from different clusters, their electronic properties can be understood on the basis of molecular orbitals (MO). The electrons of V atoms not integrated in V-S bonds localize in cluster MOs, each occupied with 7 electrons. There is one unpaired electron per V$_4$ cluster. The clusters are widely separated, hence the orbitals do not overlap with each other and the compound is nonmetallic. The electric conduction happens due to electrons hopping between the V atoms in separate $(V_4S_4)^{5+}$ clusters.

The Jahn-Teller effect drives a cubic to rhombohedral structural transition at $T_{JT} \backsimeq 42$ K, leading to a space group reduction from $Fd\bar{3}m$ to $R3m$ and the formation of a multi-domain state. The structural transition is caused by an orbital degeneracy in the asymmetrically filled electronic configuration of the V$_4$ clusters, which distorts in order to remove the degeneracy and lower the energy. Due to the Jahn-Teller distortion, the V_4 clusters are elongated along the 3-fold axis, and the distortion lowers the energy of some orbitals while raising energy of the others. The structural transition removes the degeneracy of the t_2-level (point group T_2) by splitting it into two degenerated levels: the e level with higher energy and the a_1 level with lower energy (point group C_{3v}). MO schemes of the cluster orbitals in GaV_4S_8 before and after the Jahn-Teller distortion are shown in the Figure 15. The Jahn-Teller distortion causes a dramatic increase in the the magnetic interaction at the low temperatures and GaV_4S_8 becomes ferromagnetic below $T_c = 13K$.

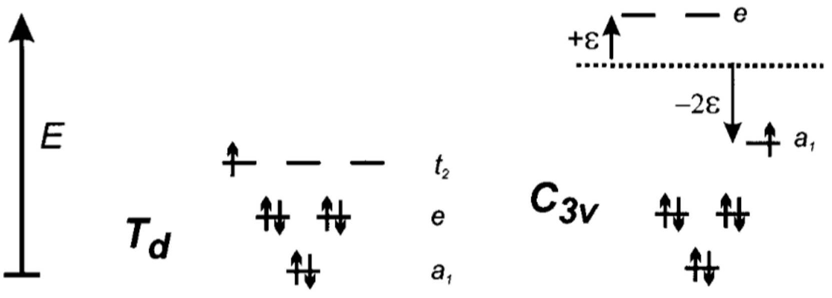

Figure 15: MO schemes of the cluster orbitals in GaV_4S_8 before and after structural transition [45].

In GaV_4S_8, the skyrmions are also generated as a result of competition between the DM interaction and ferromagnetic exchange. However, the phase diagram for GaV_4S_8 is different form that of Cu_2OSeO_3. This could be a consequence of the large uniaxial magnetic anisotropy of GaV_4S_8 caused by its rhombohedral crystal structure. Cu_2OSeO_3, on the other hand, has low magnetic anisotropy due to its cubic structure. This difference leads to an anisotropic and isotropic DM interaction for GaV_4S_8 and Cu_2OSeO_3, respectively, and can thus influence the magnetic phases in these materials. The phase diagram for GaV_4S_8 is given in Figure 16 for different applied field configurations.

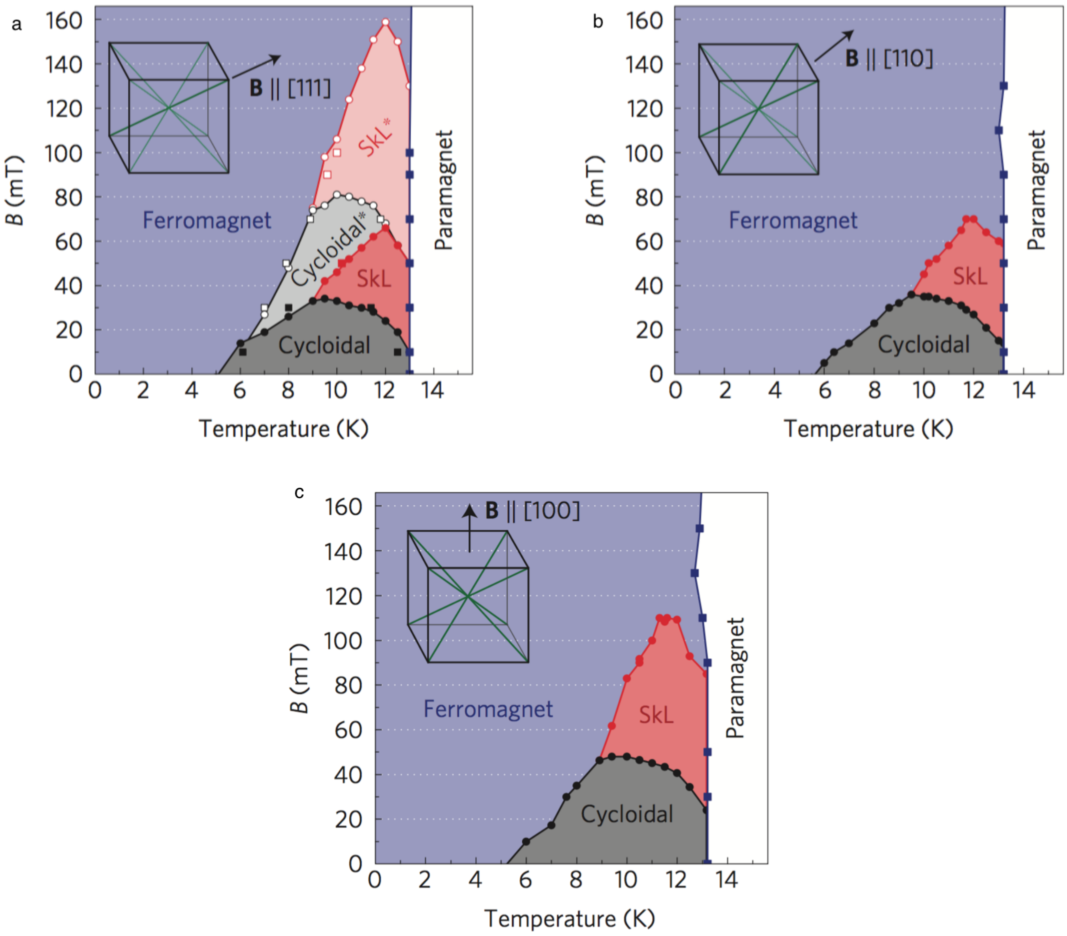

Figure 16: Magnetic phase diagram for GaV_4S_8. The insets show the orientation of magnetic field $\boldsymbol{B}$ relative to the easy axis of the different domains [19].

A new magnetic phase appears in GaV_4S_8, the so-called *cycloidal* phase. Here, the spins rotate in a plane containing the propagation vector $\boldsymbol{q}$, in contrast to the helical spin state present in Cu_2OSeO_3 where spins rotate in a plane perpendicular to $\boldsymbol{q}$. Additionally, the skyrmion phase exists over significantly broader temperature region. Moreover, due to the multi-domain state which appears after the Jahn-Teller distortion, at certain magnetic field orientations, additional phases emerge at higher B values (Figure 16 a). The differences in the magnetic phase diagram from well-studied helical magnets such as Cu_2OSeO_3, make GaV_4S_8 a particularly interesting material to investigate.

4 Experimental methods

This chapter discusses the main principles of ultrafast spectroscopy and the physics of the magneto-optic Kerr effect. The techniques employed for studying Cu_2OSeO_3 and GaV_4S_8 magnetization dynamics are also described.

4.1 Fundamentals

4.1.1 Generation of ultrashort pulses

Spectroscopy allows us to study the interaction between light and matter and is a major tool used in the study of the properties of different materials. These properties are investigated by analyzing the absorption or emission spectrum or optical properties such as the refractive index. The invention of the laser in the 1960s provided new methods to investigate various phenomena occurring in materials, and has allowed us to obtain data formerly unattainable. Lasers stimulate atoms to emit light at certain wavelengths, producing a narrow beam of electromagnetic radiation. Many types of lasers have been developed with a variety of characteristics, and the emergence of mode locking provided a method to obtain ultrashort pulses from lasers. In such mode-locked lasers, techniques such as active or passive mode locking is used to generate a train of pulses. Mode-locked lasers producing pulses in the nanosecond range were first demonstrated by Gürs and Müller with ruby lasers [46, 47] and Statz and Tang with He-Ne lasers [48]. Later, pulses were reduced to an even lower time-scale as femtosecond lasers were introduced [49].

In mode-locked laser the resonator contains an active or nonlinear passive element which leads to the generation of a short pulse traveling back and forth in the laser cavity. Every time the pulse hits an output coupler, a semi-transparent dielectric mirror, a pulse is emitted. To produce a train of ultrashort pulses in the time domain a broad bandwidth determined by a temporal duration of a pulse is required. Each mode is a solution to the Helmholtz equation that describes the laser cavity

$$\Delta E + k^2 E = 0, \tag{4.1}$$

where $k = \omega/c$ is a wavevector and E is the electric field. The frequency of the $\mathrm{n^{th}}$ mode can be represented as $\nu_n = n\frac{c}{2d}$, where n is an integer number and d is the length of the resonator. The corresponding spacing between the pulses is $\Delta\nu = \frac{c}{2d}$. For continuous wave (CW) emission, the laser's output is a superposition of a few modes around the center frequency which have random phases. The output electric field for CW operation of the laser is given by

$$E(t) = \sum_n E_n e^{i[(\omega_0 + n\Delta\omega)t + \phi_n]}, \tag{4.2}$$

where ω_0 is a center frequency and E_n, ϕ_n are the amplitude and the phase of n^{th} mode, respectively [50]. In this case, the intensity randomly fluctuates around some average value. When the laser is mode-locked, the modes have the same phase and a significant increase in intensity can be achieved. The output electric field of the mode-locked laser can be approximated by

$$E(t) \propto \frac{e^{iN\omega t} - 1}{e^{i\omega t} - 1} e^{i\omega_0 t}, \tag{4.3}$$

and the corresponding intensity is given by

$$I(t) = |E(t)|^2 \propto \frac{sin^2(N\omega t/2)}{sin^2(\omega t/2)}, \tag{4.4}$$

where N is the number of modes. There are, in general, two mode-locking schemes:

Active mode locking: In this case a loss modulator (e.g., an acousto-optic modulator) is inserted into the resonator. The modes can be locked by modulating the loss at the period which is the same as the cavity round trip time T_R. Most of the time, the loss of the cavity is kept lower than the gain except for the short period T_R . Only the pulse constructed from superposition of the modes arrives at the loss modulator in this short window of time. On each trip in the cavity the modulator cuts off the preceding and trailing parts of the pulse.

Passive mode locking: In this method, the active modulator is replaced by a saturable absorber which is a nonlinear material having an intensity dependent loss. The saturable absorber has a constant absorption for low incoming intensities. However, absorption decreases to lower values for higher intensities. Since in this technique the pulse is modulating itself, it has two major advantages: there is no need for external synchronization and the response time of the modulator is very short.

4.1.2 Dispersion compensation

The refractive index is a major parameter dictating the optical properties of any given material. Since the index of refraction of a material typically depends on frequency (i.e. materials are dispersive), there are serious consequences for pulse propagation through matter. Dispersion causes different frequencies in the wave packet of the pulse to propagate with different speeds. Thus, broadening of the temporal intensity profile occurs.

The time delay experienced by the ultrafast pulses in various optical devices is described by the *group delay* (GD)

$$T_g = \frac{\partial \varphi(\omega)}{\partial \omega}, \tag{4.5}$$

where φ is the spectral phase evolving with frequency as

$$\varphi(\omega) = \frac{\omega n(\omega) L}{c}. \tag{4.6}$$

Here $n(\omega)$ is refractive index and L is the propagation length.

Expansion of the phase around the center frequency ω_0 gives

$$\begin{aligned}\varphi(\omega) &\backsimeq \frac{L}{c}\left[\varphi_0 + (\omega-\omega_0)\left(\frac{\partial\varphi}{\partial\omega}\right)_{\omega_0} + \frac{(\omega-\omega_0)^2}{2}\left(\frac{\partial^2\varphi}{\partial\omega^2}\right)_{\omega_0} + ...\right] \\ &= \frac{L}{c}\left[\varphi_0 + (\omega-\omega_0)\,T_g + \frac{(\omega-\omega_0)^2}{2}\mathrm{GDD} + ...\right], \end{aligned} \tag{4.7}$$

where $\mathrm{GDD} = \left(\frac{\partial^2\varphi}{\partial\omega^2}\right)_{\omega_0} = \left(\frac{\partial T_g}{\partial\omega}\right)_{\omega_0}$ is the *group delay dispersion.* GDD governs the dominant broadening or compression of the pulse.

The expected values of GD and GDD for an optical path $P = nL$ can be calculated using the equations

$$T_g(\omega) = \frac{P}{c} + \frac{\omega}{c}\frac{dP}{d\omega}, \tag{4.8}$$

$$\mathrm{GDD} = \frac{1}{c}\left(2\frac{dP}{d\omega} + \omega\frac{d^2P}{d\omega^2}\right). \tag{4.9}$$

Propagation of a pulse through a medium with positive dispersion causes the low frequency components to outrun the higher frequency components, while negative dispersion leads to the opposite effect. Hence, balance of the negative and positive dispersion has to be achieved so that the higher frequency components will catch up with the low frequency components or vice versa.

In mode-locked lasers with pulse durations less than roughly 25 fs, one has to provide dispersion compensation not only for GDD, but also (ideally) for third order dispersion (TOD)

$$\mathrm{TOD} = \left(\frac{\partial^3\varphi}{\partial\omega^3}\right)_{\omega_0} = \left(\frac{\partial^2 T_g}{\partial\omega^2}\right)_{\omega_0}. \tag{4.10}$$

The corresponding change in the spectral phase is given by

$$\Delta\varphi = \frac{L}{6c}(\omega-\omega_0)^3 \cdot \mathrm{TOD}. \tag{4.11}$$

In order to achieve dispersion compensation one can use optical schemes such as prism compressor. It is an optical device which consists of two prisms and a mirror. If the different frequency components of a laser pulse are separated in time, the prism compressor can make them overlap with each other, thus causing a shorter pulse and achieve the GDD matching via adjusting the distance between the prisms and prism insertion. Since one can also choose between different prism materials, the optimal dispersion compensation can be achieved. Moreover, one can use low GDD optics such as mirrors, beam splitters etc. in order to avoid the drastic pulse broadening.

4.1.3 Magneto-optic Kerr effect

The magneto-optic Kerr effect (MOKE) describes the changes in the polarization and intensity of the light reflected from a magnetized surface. MOKE is the phenomenological analog to the Faraday effect, describing the changes in the properties of the light transmitted through a magnetic material. Both effects originate from the off-diagonal components of the dielectric tensor ε. The Kerr or Faraday rotation can be measured in different geometries classified by the direction of the magnetization vector $\mathbf{M}$ (Figure 17). Under appropriate conditions, the MOKE signal is proportional to the magnetization $\mathbf{M}$, thus one can use this technique in order to optically probe the magnetization of the sample.

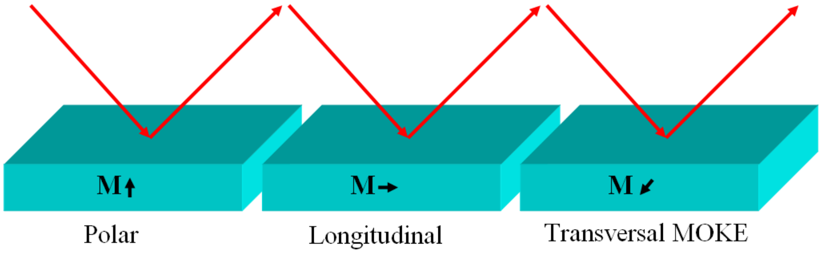

Figure 17: Different MOKE geometries depending on the orientation of the incoming light and the magnetization direction of the sample: longitudinal, polar and transverse.

The general form of the dielectric tensor can be written as

$$\varepsilon(\omega)=\begin{pmatrix}\varepsilon_{xx} & \varepsilon_{xy} & \varepsilon_{xz}\\ \varepsilon_{yx} & \varepsilon_{yy} & \varepsilon_{yz}\\ \varepsilon_{zx} & \varepsilon_{zy} & \varepsilon_{zz}\end{pmatrix}. \tag{4.12}$$

For some crystal systems (e.g., cubic), this matrix can be diagonalized so that non-diagonal elements vanish

$$\varepsilon(\omega)=\begin{pmatrix}\varepsilon_{xx} & 0 & 0\\ 0 & \varepsilon_{yy} & 0\\ 0 & 0 & \varepsilon_{zz}\end{pmatrix}. \tag{4.13}$$

If the relationship between the the matrix elements is $\varepsilon_{xx} \neq \varepsilon_{yy} \neq \varepsilon_{zz}$, the crystal is biaxial and if $\varepsilon_{xx} = \varepsilon_{yy} \neq \varepsilon_{zz}$, it is uniaxial. When all diagonal matrix elements are equal to each other, the crystal is cubic. In the simpler cases of cubic (4.14) and uniaxial (4.15) crystals, the refractive indices are given by

$$n=\sqrt{\varepsilon}; \varepsilon_{yy}=\varepsilon_{zz}=\varepsilon, \tag{4.14}$$

$$n_{\mathrm{o}}=\sqrt{\varepsilon_1}, n_{\mathrm{e}}=\sqrt{\varepsilon_2}, ; \varepsilon=\varepsilon_{yy}=\varepsilon_{1,}\varepsilon_{zz}=\varepsilon. \tag{4.15}$$

In the equation (4.15), n_{o} is the ordinary refractive index and n_{e} is the extraordinary refractive index.

In the presence of a finite magnetization, the off-diagonal components of the dielectric tensor become non-zero. These off-diagonal components induce the Kerr and Faraday effects and appear in the dielectric tensor because time-reversal symmetry in the material is broken. One can consider a dielectric tensor (equation (4.16)) for a cubic material with non-zero diagonal elements ($\mathbf{M}$ is along z, polar geometry) in order to derive the expressions for the Kerr and Faraday rotations and ellipticities, the measured quantities in our experiment. Such a tensor is given by

$$\varepsilon(\omega)=\begin{pmatrix}\varepsilon_{xx} & \varepsilon_{xy} & 0\\ -\epsilon_{yx} & \varepsilon_{yy} & 0\\ 0 & 0 & \varepsilon_{zz}\end{pmatrix}, \tag{4.16}$$

where the complex matrix elements ε_{ij} are $\varepsilon_{ij} = \varepsilon'_{ij} + i\varepsilon''_{ij}$. The presence of the off-diagonal elements yields different responses to right (RCP) and left circularly polarized (LCP) light [50]. The two circularly polarized waves will propagate with different dielectric constants $\varepsilon_+$and ε_-, and thus different complex refractive indices $n_+ = n'_+ + in''_+$ and $n_- = n'_- + in''_-$. The relation between the refractive indices and matrix elements is given by

$$\varepsilon_{\pm} = \varepsilon_{xx} + i\varepsilon_{xy} = (n'_{\pm} + in''_{\pm})^2. \tag{4.17}$$

LCP and RCP light waves propagate with different phase velocities and the difference between ε_+ and ε_- is the origin of the polarization rotation and ellipticity. One can define a complex MOKE angle (Voigt vector) as

$$\tilde{\Theta}_{\mathrm{k}} = \theta_{\mathrm{k}} + i\eta_{\mathrm{k},} \tag{4.18}$$

where θ_k is the Kerr rotation and η_k is ellipticity. The connection between the Voigt vector and the dielectric tensor components is given by (derivation is given in Appendix A.1)

$$\tilde{\Theta}_{\mathrm{k}} = \frac{-\varepsilon_{xy}}{\sqrt{\varepsilon_{xx}}(\varepsilon_{xx} - 1)}. \tag{4.19}$$

Similarly, one can express a complex Faraday angle for polar geometry (at normal incidence) as [51]

$$\tilde{\Theta}_{\mathrm{f}} = \theta_{\mathrm{f}} + i\eta_{\mathrm{f}} = \frac{\omega d}{2c} \frac{i\varepsilon_{xy}}{\sqrt{\varepsilon_{xx}}}, \tag{4.20}$$

where ω is the frequency of the transmitted light wave and d is the thickness of the material.

4.1.4 Photoelastic modulator (PEM)

In general, a transparent crystal becomes birefringent under stress. In photoelastic modulator, this effect causes different polarizations of light to travel at different speeds when passing through the quartz element. When the quartz element is compressed, the polarization component parallel to the PEM axis travels slightly faster than the one perpendicular to it. The phase difference at any instant between these components is called the retardation. When the peak retardation is $\lambda/2$, the PEM acts like a half-wave plate, and when it is $\lambda/4$ - like a quarter-wave plate. Figure (18) shows how the incoming linear polarization is modulated at $\lambda/4$ retardation. The polarization oscillates between RCP and LCP, with linear and elliptical polarization states in between. By placing the PEM between crossed polarizers, both oriented at 45^0relative to the PEM axis, the result is light whose intensity is modulated at twice the PEM drive frequency.

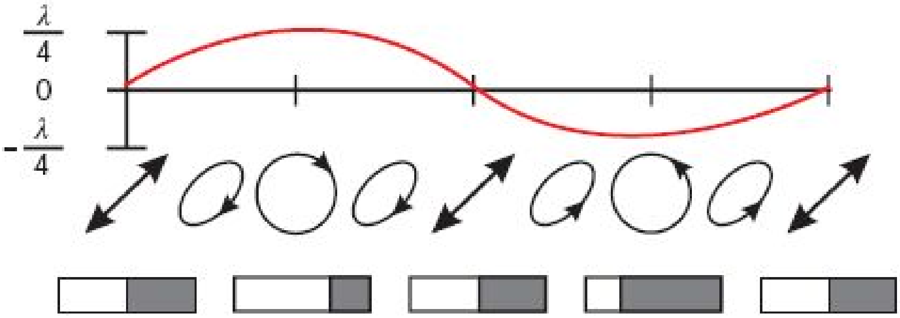

Figure 18: Polarization modulation at $\lambda/4$ retardation.

4.2 Single modulation pump-probe technique

Pump-probe spectroscopy is the most common experimental technique used for studying the ultrafast dynamics of a material. In this method, a laser pulse train is split into two separate beams, referred to as pump and probe. A stronger pulse (pump) excites the sample, while a weaker pulse (probe) is used to monitor the pump-induced changes in the optical properties. The probe beam is focused onto the sample so that it is spatially overlapped with the focused pump beam spot. The probe spot is smaller to ensure that the probe measures a relatively homogeneous pump excitation. The changes in reflectivity or transmission of the material as a function of time delay between the arrival of pump and probe pulses provides information about the processes happening in the sample. The schematic of a pump-probe setup is given in Figure 19.

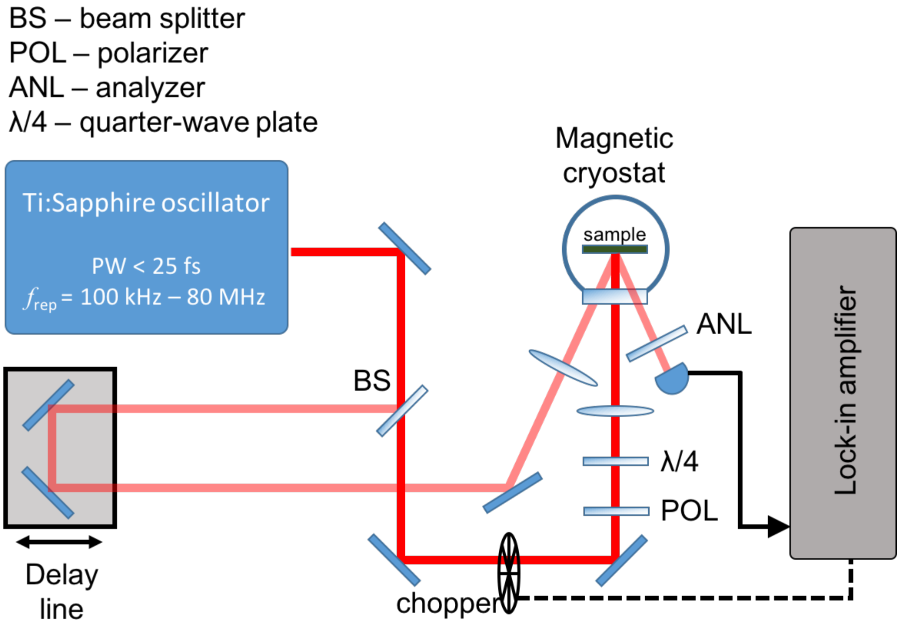

Figure 19: Schematic of the single modulation pump-probe setup.

In our setup we use a Ti:sapphire laser (KM Cascade) with repetition rate varying from 100 kHz to 80 MHz with pulse energy up to 40 nJ/pulse. With appropriate pulse compression, a pulse width of less than 25 fs can be achieved. The pump beam is chopped in order to modulate pump-induced change in the transmitted or reflected probe beam power at frequency f_c. In this way both the pump and probe beams have a component at the frequency f_c, but only the modulated component of the probe beam carries the signal of interest. The mechanical chopper frequency which modulates the pump beam, serves as the reference for the lock-in amplifier (Stanford Research SR830 or SR844), which then allows us to detect the component at f_c that exists in the reflected probe. In a degenerate pump-probe setup, both the pump and the probe beams have the same wavelengths. This makes separating measured probe beam from the scattered pump beam after the reflection from or transmission through the sample difficult, and results in a significant background signal on the detector. For materials that yield weak pump-induced changes, this can be a significant hurdle in achieving a high quality signal.

4.3 Double modulation technique using the polarization bridge

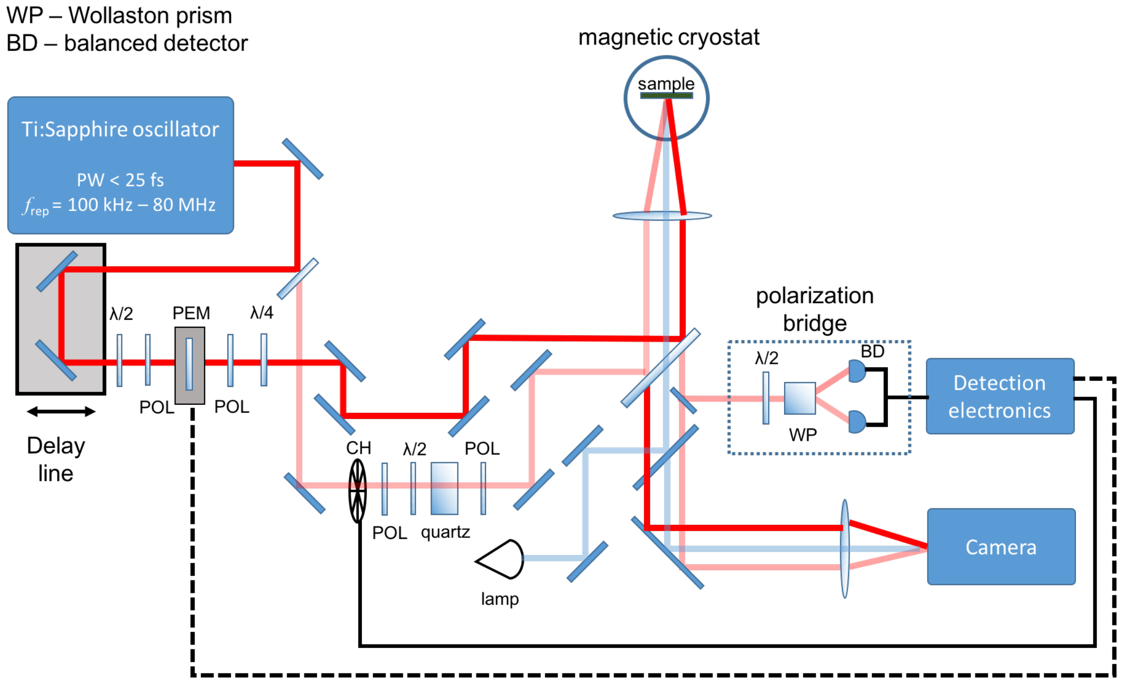

Figure 20: Double-modulation TR-MOKE setup using polarization bridge for detection.

In this setup, schematically depicted in Figure 20, double modulation can be used to overcome some of the pitfalls of the single modulation scheme. The chopper now is in the probe path, and the PEM is in the pump path. To simplify the description of the setup, the pump and probe paths are discussed separately:

Pump path: The pump goes through a half-wave plate, which rotates the plane of polarization of the incoming beam parallel to the vertical axis. Next, the light goes through the polarizer oriented such that only vertically polarized light passes through, and then goes through the PEM whose axis is oriented at 45^0 to the vertical axis. Hence, the difference between the vertically polarizied light and the PEM axis is 45^0. The PEM is set to have the quarter-wave retardation, such that the output beam polarization changes from linear to right circular, then back to linear (now 90^0 with respect to the initial linear polarization), then to left circular and so on. The light then travels through a polarizer oriented such that only horizontally polarized light can pass it. Hence, PEM in this setup is used like a chopper operated at high frequency (100 kHz) imparting a nearly sinusoidal modulation on the pump beam. The beam then goes through a quarter-wave plate, which can either preserve the linear polarization or convert it into circular polarized light. Next, the light passes through a beam splitter, with the transmitted portion being dumped, and reflected component focused onto the sample contained within a magnetic cryostat (Oxford Instruments magnetostat).

Probe path: The probe light also goes through the half-wave plate and then it passes through a polarizer oriented such that only the vertically polarized light is transmitted. Next, it passes through a piece of quartz compensating for the GDD from the PEM. Next, a second half-wave plate, is used to rotate the plane of polarization. Finally, the probe light is focused on the sample with the same optics used for the pump beam.

We detect the reflected probe light which contains information on the processes induced by the pump. The reflected probe is analyzed using a *polarization bridge*. The first part of this bridge is a half-wave plate, which rotates the plane of polarization of the probe beam such that its polarization is at 45^0 (in absence of the pump and B=0) with respect to the axis of the Wollaston prism. The Wollaston prism then splits the light into equivalent vertical and horizontal components. Now, if the polarization coming to a half-wave plate is slightly rotated, the vertically and horizontally polarized light coming out of the prism will be of slightly different intensity. This difference is the signal of interest, corresponding to the Kerr rotation. The polarization split probe beams then go to independent channels of the balanced detector, which subtracts input of channel B from the input of channel A. The difference (A-B) is then sent to *cascaded lock-in amplifiers* (see Figure 21).

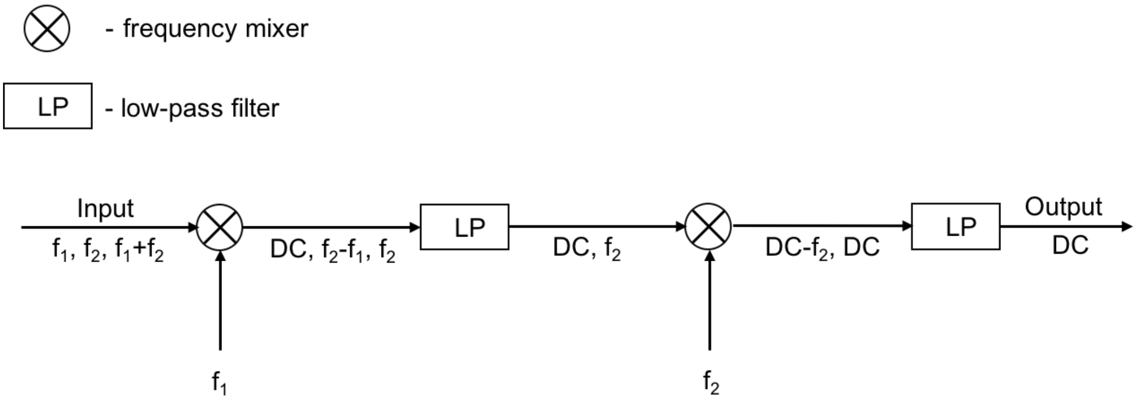

Figure 21: Cascaded lock-in amplifiers.

In the cascaded lock-in system, the signal, which contains the frequency components f_1 (PEM), f_2 (chopper) and $f_1 + f_2$ (signal of interest), goes to the first lock-in, referenced at f_1. The frequency components of the signal are then mixed with an internally generated reference signal at f_1. The f_1 component in the original input is shifted to DC, and the to other two components shift such that: $f_2 \to f_2 - f_1$,$f_1 + f_2 \to f_2$. One has to choose the parameters of the lock-ins' low pass filter in order to pass the desirable frequencies. The pass band is primarily determined by the *time constant* and ideally the dependence of the signal attenuation with respect to frequency should resemble a step function as much as possible. This closeness to a step function is set by the *dB roll-off* of the lock-in. One has to make sure that the frequency f_2 falls in the pass band by setting the time constant of the first lock-in τ_1 to be sufficiently small, and f_2 to be sufficiently low. Since frequency of the PEM is much larger then the frequency of the chopper, the output of the first lock in will contain the DC and f_2 frequency components only. This signal is then sent to the second lock in where its frequency components are mixed with a reference signal at f_2. The output components then are DC-f_2 and DC. The time constant of the second lock-in (τ_2) is set in a way that the pass band is very narrow. The output signal is then DC, which corresponds to the original $f_1 + f_2$ signal.

5 Results and discussion

5.1 Jahn-Teller driven ferroelectric transition of GaV_4S_8

In most cases ferroelectricity emerges due to the structurally driven displacement of ions. However, there are other mechanisms which can lead to ferroelectricity, including orbital order [52]. Since Jahn-Teller transition leads to long-range orbital ordering of the system, it can lead to the ferroelectric polarization of the system. Few ferroelectric Jahn-Teller materials were studied until recently [53, 54]. Ferroelectricity driven by Jahn-Teller distortion can appear in lacunar spinels, including GaV_4S_8 [55, 56]. We conducted Raman and time-resolved differential reflectivity measurements in order to attempt to determine the phonon modes involved in the Jahn-Teller ferroelectric transition.

5.1.1 Raman spectrum of GaV_4S_8

Raman spectroscopy is a technique based on inelastic scattering of monochromatic light from a sample and measures the quasi-particle excitations, such as quantized vibrations of the lattice. Raman scattering was discovered by C. V. Raman and K. S. Krishnan in liquids (1928) and was also reported for crystals by G. Landsberg and L. Mandelstam [57, 58]. In contrast to the strong elastic Rayleigh scattering, which has the frequency of the incident light f_0, inelastic Raman scattering is comparatively weak and has frequency $f_0 \pm f_m$, where f_m is, for example, the frequency of a molecular vibration. In Raman spectroscopy one measures the frequencies f_m as a shift from f_0. The spectral lines corresponding to $f_0 + f_m$ and $f_0 - f_m$ are called Stokes (excitations are created during this process) and anti-Stokes (excitations are annihilated), respectively. The basics of inelastic scattering can be explained classically, which is the approach chosen here.

In the classical description, the oscillating electric field of incident photons is given by

$$\boldsymbol{E} = \boldsymbol{E}_0 cos(2\pi f_0 t). \tag{5.1}$$

This field induces the dipole moment $\boldsymbol{P}$ of the molecule

$$\boldsymbol{P} = \alpha \boldsymbol{E}, \tag{5.2}$$

where α is the polarizability, which measures the ease with which the electrons around the molecule can be distorted. Raman scattering occurs because the polzarizability can be changed by the vibrations of the molecule. If α is small, it can be extended as a Taylor series in displacements $q = q_0 cos(2\pi f_m t)$, where q_0 is the vibrational amplitude of the molecule:

$$\alpha = \alpha_0 + \left(\frac{\partial\alpha}{\partial q}\right)_{q_0} \cdot q_0 + \frac{1}{2}\left(\frac{\partial^2\alpha}{\partial q^2}\right)_{q_0} \cdot q_0^2 + ... \tag{5.3}$$

In the equation (5.3) α_0 is the polarizability at equilibrium position.

Plugging (5.1) and (5.3) into (5.2) (considering only the first two terms) one gets the following expression for the dipole moment:

$$P = \alpha_0 E_0 cos(2\pi f_0 t) + \frac{1}{2}\left(\frac{\partial\alpha}{\partial q}\right)_{q_0} \cdot q_0 E_0 \left\{cos[2\pi(f + f_0)t] + cos[2\pi(f - f_0)t]\right\}, \tag{5.4}$$

where the second and third terms correspond to Stokes and anti-Stokes processes. The scattered light intensity is proportional to P^2 and E^2.

Due to classic considerations, the relation between Stokes and anti-Stokes intensities should be of the following form:

$$\frac{I_{Stokes}}{I_{anti-Stokes}} = \frac{(f_0 - f_m)^4}{(f_0 + f_m)^4}. \tag{5.5}$$

The quantum-mechanical approach provides the correction to equation (5.5), and the new intensity relation is

$$\frac{I_{Stokes}}{I_{anti-Stokes}} = \frac{(f_0 - f_m)^4}{(f_0 + f_m)^4} exp\left(-\frac{hf_m}{kT}\right). \tag{5.6}$$

One can determine the temperature associated with the excitation using equation (5.6).

The small lattice oscillations can be expressed in terms of *normal modes.* These modes are independent from each other and their energies are quantized. The quantum of a lattice vibration is a phonon. For crystals with more than one atom in the unit cell, there are two types of phonons: acoustic and optical. For *acoustic modes*, the neighboring atoms are in phase and in the long-wavelength limit they correspond to the sound-waves. In contrast, the neighboring atoms are out of phase for the *optical modes.* There are two types within each mode: longitudinal mode with displacements parallel to the direction of propagation and transverse mode with displacements perpendicular to the direction of propagation. Hence, four different modes exist: transverse acoustic (TA), longitudinal acoustic (LA), transverse optical (TO), and longitudinal optical (LO). Optical modes with nonzero wave vector $\boldsymbol{q}$ can be LO or TO, depending on how the displacement is oriented with respect to $\boldsymbol{q}$. If the modes are not polarized, the LO and TO components are degenerate. Since the LO phonon supports a longitudinal electric field, there is an additional Coulomb restoring force for the LO phonon modes, and the LO and TO modes are no longer degenerate - the LO frequency is always higher than TO frequency. The difference between the longitudinal and transverse mode frequency is called *LO-TO splitting* [59, 60]. Optical phonons can interact with light and the active modes can be infrared (IR) active and/or Raman active . Polar modes are always IR active. For non-centrosymmetric materials, the modes can be both IR and Raman active. The activity of the modes is determined by the crystal symmetry. Modes are IR active if they transform as vectors x, y or z, and are Raman active if they transform as the product of vectors x, y or z (quadratic functions such as $x^2, x^2 - y^2$ and so on). The activity of modes can be obtained from a character table for the point group of a particular material. In case of $GaV_4S_{8,}$ the point group is T_d in the paraelectric phase (above the JT transition temperature). After the structural transition at T_{JT}, the symmetry reduces to C_{3v} (rhombohedral, space group $R3m$). The character tables for T_d and C_{3v} are shown in the table 1 and table 2, respectively.

T_d	E	$8C_3$	$3C_2$	$6S_4$	$6\sigma_d$	Linear functions, rotations	Quadratic functions
A_1	+1	+1	+1	+1	+1	-	$(x^2 + y^2 + z^2)$
A_2	+1	+1	+1	-1	-1	-	-
E	+2	-1	+2	0	0	-	$(2z^2 - x^2 - y^2, x^2 - y^2)$
T_1	+3	0	-1	+1	-1	(R_x, R_y, R_z)	-
T_2	+3	0	-1	-1	+1	(x, y, z)	(xy, xz, yz)

Table 1: Character table for T_d point group. The first column gives the irreducible representations of the group. The first row reads the following from left to right: the notation of the group; its symmetry elements (five of them for T_d) ; linear functions and rotations (linear functions give information about IR activity); quadratic functions (give information about Raman activity).

C_{3v}	E	$2C_3(z)$	$3\sigma_v$	Linear functions, rotations	Quadratic functions
A_1	+1	+1	+1	z	$x^2 + y^2, z^2$
A_2	+1	+1	-1	R_z	-
E	+2	-1	0	$(x, y), (R_x, R_y)$	$(x^2 - y^2, xy), (xz, yz)$

Table 2: Character table for C_{3v} point group. Should be read as the table 1.

The Wyckoff positions of the Ga, V, and S atoms in the paraelectric phases are $4a$, $16e$, and $16e$, respectively. There are 13 atoms per unit cell, thus the number of normal modes for GaV_4S_8 is $3N = 3 \cdot 13 = 39$. Three of these modes are acoustic

(T_2 symmetry) and the rest are optic. Group theory predicts the following optical modes for T_d at the gamma point:

$$\Gamma = 3A_1 + 3E + 3T_1 + 6T_2, \tag{5.7}$$

where A_1 modes are singly degenerate, E are doubly degenerate, and T_1 and T_2 are triply degenerate, which gives 36 optical modes in total. The modes A_1, E and T_2 transform like a product of two vectors and are Raman active, as can be seen from the table 1. After the structural transition $T_d \to C_{3v}$, T_1 modes split into modes A_2 and E, and T_2 modes into modes A_1 and E. The normal modes at the gamma point predicted by group theory are then

$$\Gamma = 9A_1 + 3A_2 + 15E, \tag{5.8}$$

where the new mode A_2 is singly degenerate and Raman inactive (see table 2). The Raman tensors corresponding to the active modes were rotated to the basis in which the experiment was conducted. In our case, the light was scattered from the (111) crystal facet (as shown in Figure 22) and the normalized basis vectors were

$$\begin{aligned} x' &= \frac{1}{\sqrt{2}}[1\bar{1}0], \\ y' &= \frac{1}{\sqrt{6}}[11\bar{2}], \\ z' &= \frac{1}{\sqrt{3}}[111]. \end{aligned} \tag{5.9}$$

The measurements were done with the polarization of the incident light along the x direction, and the scattered light along the x or y direction for the parallel or crossed configuration, respectively.

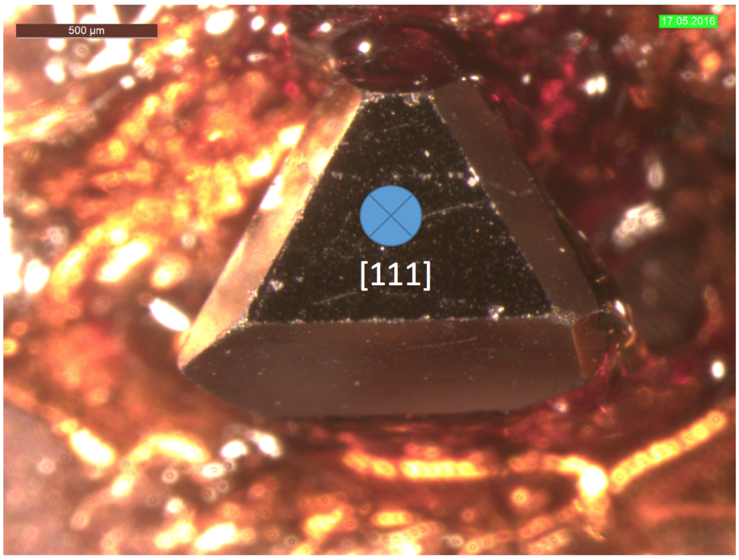

Figure 22: The (111) GaV_4S_8 sample.

The rotated Raman tensors for modes of the T_d point group are

$$R(A_1) = \begin{pmatrix} a & 0 & 0 \\ 0 & a & 0 \\ 0 & 0 & a \end{pmatrix}, R(E(1)) = \begin{pmatrix} b & 0 & 0 \\ 0 & -b & \sqrt{2}b \\ 0 & \sqrt{2}b & 0 \end{pmatrix},$$

$$R(E(2)) = \begin{pmatrix} 0 & -b & -\sqrt{2}b \\ -b & 0 & 0 \\ -\sqrt{2}b & 0 & 0 \end{pmatrix}, \tag{5.10}$$

$$R(T_2(x)) = \begin{pmatrix} 0 & \frac{d}{\sqrt{3}} & -\frac{d}{\sqrt{6}} \\ \frac{d}{\sqrt{3}} & -\frac{2d}{3} & -\frac{\sqrt{2}d}{6} \\ -\frac{d}{\sqrt{6}} & -\frac{\sqrt{2}d}{6} & \frac{2d}{3} \end{pmatrix}, R(T_2(y)) = \begin{pmatrix} 0 & -\frac{d}{\sqrt{3}} & \frac{d}{\sqrt{6}} \\ -\frac{d}{\sqrt{3}} & -\frac{2d}{3} & -\frac{\sqrt{2}d}{6} \\ \frac{d}{\sqrt{6}} & -\frac{\sqrt{2}d}{6} & \frac{2d}{3} \end{pmatrix},$$

$$R(T_2(z)) = \begin{pmatrix} -d & 0 & 0 \\ 0 & \frac{d}{3} & \frac{\sqrt{2}d}{3} \\ 0 & \frac{\sqrt{2}d}{3} & \frac{2d}{3} \end{pmatrix}.$$

The rotated tensors for the Raman active modes of the C_{3v} point group are

$$R(A_1(z)) = \begin{pmatrix} a & 0 & 0 \\ 0 & \frac{1}{3}(a+2b) & \frac{\sqrt{2}}{3}(a-b) \\ 0 & \frac{\sqrt{2}}{3}(a-b) & \frac{1}{3}(2a+b) \end{pmatrix}$$

$$R(E(x)) = \begin{pmatrix} -c & -\frac{d}{\sqrt{3}} & \frac{d}{\sqrt{6}} \\ -\frac{d}{\sqrt{3}} & \frac{1}{3}(c-2d) & \frac{\sqrt{2}}{6}(2c-d) \\ \frac{d}{\sqrt{6}} & \frac{\sqrt{2}}{6}(2c-d) & \frac{2}{3}(c+d) \end{pmatrix}, \tag{5.11}$$

$$R(E(y)) = \begin{pmatrix} 0 & \frac{1}{\sqrt{3}}(c+d) & \frac{1}{\sqrt{6}}(2c-d) \\ \frac{1}{\sqrt{3}}(c+d) & -\frac{2d}{3} & -\frac{\sqrt{2}d}{6} \\ \frac{1}{\sqrt{6}}(2c-d) & -\frac{\sqrt{2}d}{6} & \frac{2d}{3} \end{pmatrix}.$$

The details of the Raman tensor rotation from cartesian to the new basis are given in Appendix A.2.

The selection rules for spontaneous Raman scattering are given by

$$I_s \propto \left| \boldsymbol{e}_s \cdot \overleftrightarrow{R} \cdot \boldsymbol{e}_i \right|^2, \tag{5.12}$$

where $\boldsymbol{e}_i$ and $\boldsymbol{e}_s$ are the unit polarization vectors for incident and scattered light, respectively. The allowed phonon modes for both T_d and C_{3v} symmetries are given in the tables 3 and 4, respectively.

Allowed modes (T_d)	
Cross	Parallel
$E(2)$,$T_2(x)$,$T_2(y)$	A_1,$E(1)$,$T_2(z)$

Table 3: Allowed phonon modes for T_d symmetry (cross and parallel polarization configurations).

Allowed modes (C_{3v})	
Cross	Parallel
$E(x)$,$E(y)$	$A_1(z)$,$E(x)$

Table 4: Allowed phonon modes for C_{3v} symmetry (cross and parallel polarization configurations).

The Raman spectrum (Stokes and anti-Stokes) was measured for different values of optical density (OD) in cross and parallel polarization configurations, and the lattice temperature of the sample at every OD was determined from the ratio of intensities of the strongest phonon peaks in the Stokes and anti-Stokes spectra. Since the calculated temperatures for cross and parallel polarizations at the same OD values varied slightly, the average values of the two temperatures were taken.

Figures 23 and 24 show the spectra at 100% transmission (OD=0, 5.3 mW) for the cross and parallel polarization configurations, respectively. The modes were assigned using the calculated selection rules and results recently reported in the literature (Figure 25, table 7).

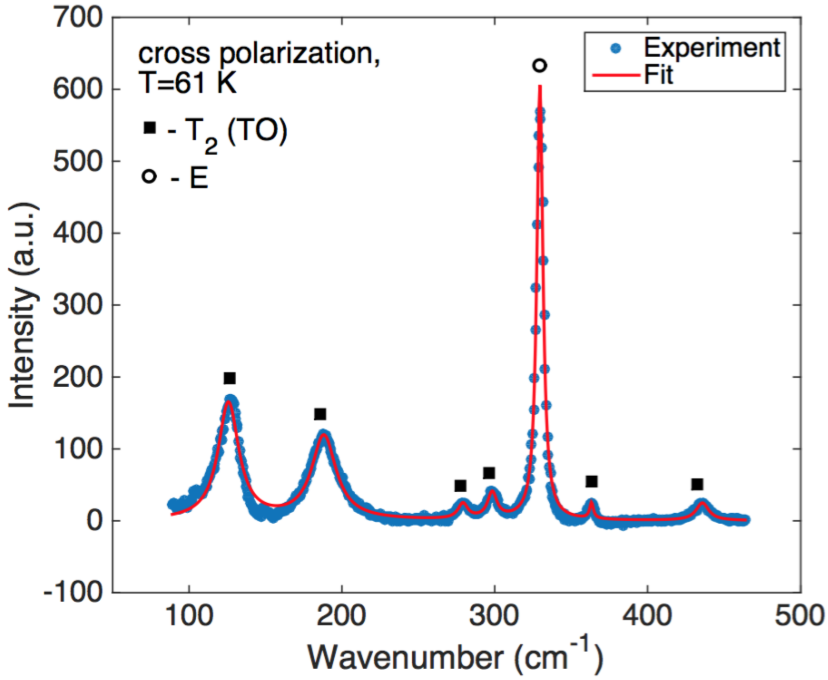

Figure 23: Raman spectrum at T=61 K (cross polarization configuration).

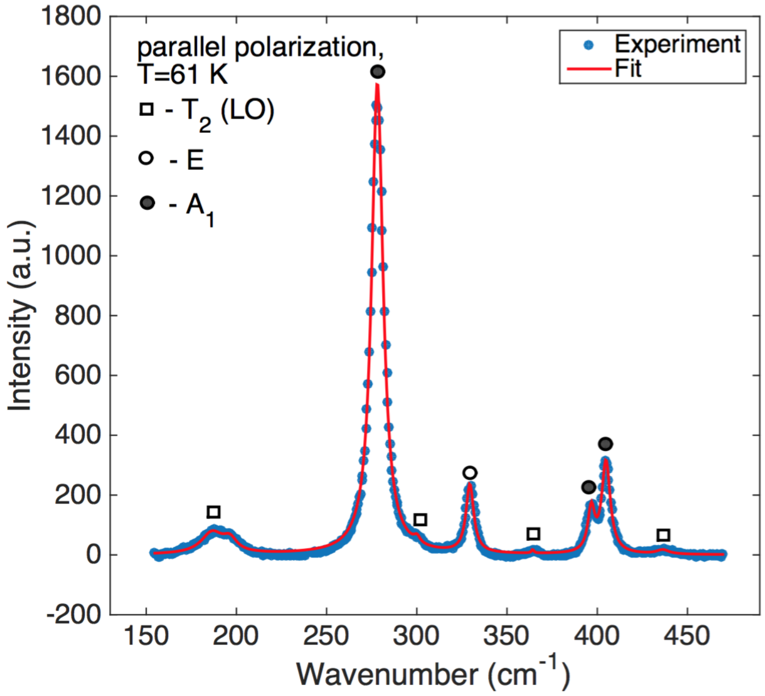

Figure 24: Raman spectrum at T=61 K (parallel polarization configuration).

Since we measured Raman spectra in the backscattering geometry, wave vector conservation requires

$$\boldsymbol{k}_s = \boldsymbol{k}_i - \boldsymbol{q}, \tag{5.13}$$

where $\boldsymbol{k}_i$,$\boldsymbol{k}_s$, and $\boldsymbol{q}$ are the wave vectors of the incident light, scattered light, and the phonon, respectively. The incident (and scattered) light was along z axis. Thus, according to the calculated selection rules, in the paraelectric T_d phase only the T_2(TO) phonons should be observed for the cross polarization configuration, and only the T_2(LO) phonons for the parallel polarization configuration (see table 3). In the cross polarization configuration, only the E mode, corresponding to the rotated Raman tensor $E(2)$, and the T_2(TO) mode are allowed. The strongest peak in Figure 23 was assigned to the E mode from comparison with literature (Figure 25) and the fact that it disappears in the parallel configuration. In the parallel polarization configuration (Figure 24), the selection rules predict modes A_1 and $E(1)$ in addition to the T_2 (LO) mode. In this case, the modes were assigned through comparison with literature. The peak positions of the Raman spectra at T=61 K for the cross and parallel polarization configurations are summarized in tables 5 and 6, respectively. The peaks observed in our measurements are slightly redshifted in comparison to the ones reported in [52], which could be caused by the difference in the temperatures at which the spectra were obtained. The broad T_2(LO) peak (parallel polarizaton) at 187 cm^{-1}has a bump at 197 cm^{-1} which is most likely due to leakage scattering of a T_2(TO) mode. A new feature was observed at 300 cm^{-1} (T_2(LO)) as a shoulder of the strongest peak at 278 cm^{-1}(A_1) in the parallel polarization configuration.

Mode	T_2 (TO)				E	T_2 (TO)	
Peak position (cm^{-1})	126	188	279	298	330	363	436

Table 5: Phonon modes of GaV_4S_8observed at 61 K for cross polarization configuration.

Mode	T_2 (LO)	A_1	T_2 (LO)	E	T_2 (LO)	A_1	A_1	T_2 (LO)
Peak position (cm^{-1})	187	278	300	329	364	397	405	436

Table 6: Phonon modes of GaV_4S_8observed at 61 K for parallel polarization configuration.

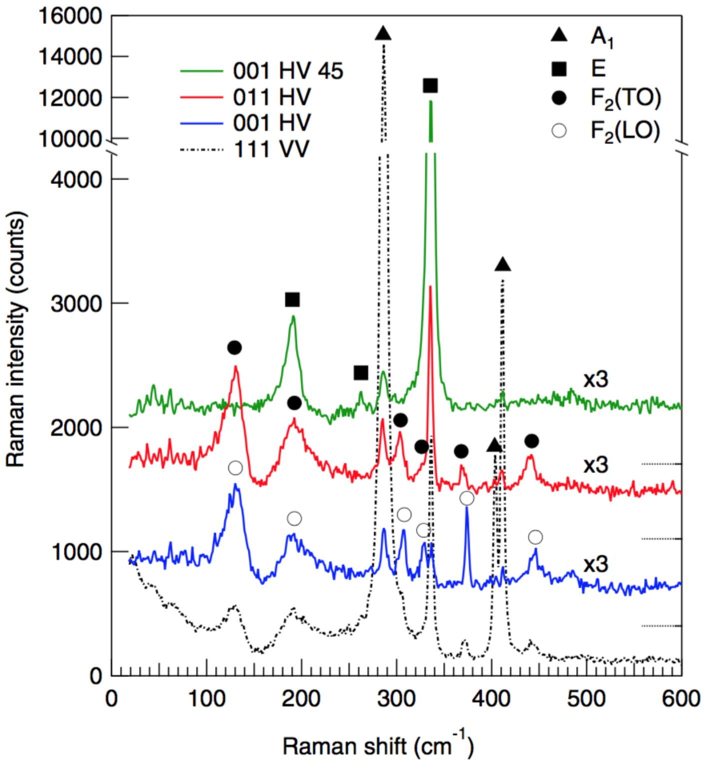

Figure 25: Raman spectra for scattering from crystal facets with (111), (011), (001). Polarization configurations:(111) - parallel; (011) - cross and at 45^0; (001) - cross [52].

	Raman (80 K)		IR (80 K)		Theory (0 K)		Comment
	TO	LO	TO	LO	*E*	A_1 (A_2)	
F_2	442	445	441	442	440	462	Asym. stretch
A_1	411					419	V_4S_4 breathing
A_1	404					367	GaS_4 breathing
F_2	371	374	370	373	336	343	Asym. stretch
E	336				338		
F_2		328	314	326	285	292	Strongest IR
F_2	304	307	303	307	331	326	
F_1					305	(314)	Rotational
A_1	287					287	Stretch
E	263				250		
F_1					220	(222)	Rotational
F_2	193	193			169	**203**	V_4 JT mode
E	190				207		
F_1					142	(141)	Rotational
F_2	130	130			114	**133**	Ga-V_4S_4

Table 7: Phonon modes of GaV$_4$S$_8$reported in literature (observed at 80 K and theoretically predicted for 0 K). Geometry of the measurements: scattering from crystal facets with (111), (011), (001). Polarization configurations:(111) - parallel; (011) - cross and at 45^0; (001) - cross [52].

The spectra at 25 K in the cross and parallel polarization configurations are shown in the Figures 26 and 27, respectively. Due the reduction of symmetry from T_d to C_{3v}, one should observe the splitting of the T_1 modes into A_2 and E modes, and T_2 into A_1 and E. However, we did not observed this splitting and the spectra did not change significantly, apart from a slight shift of the peak positions and the new feature at 323 cm^{-1} (T_2) forming a shoulder of the peak at 329 cm^{-1} (E). The peak positions of the Raman spectra at T=25 K for cross and parallel polarization configurations are summarized in the tables 8 and 9, respectively.

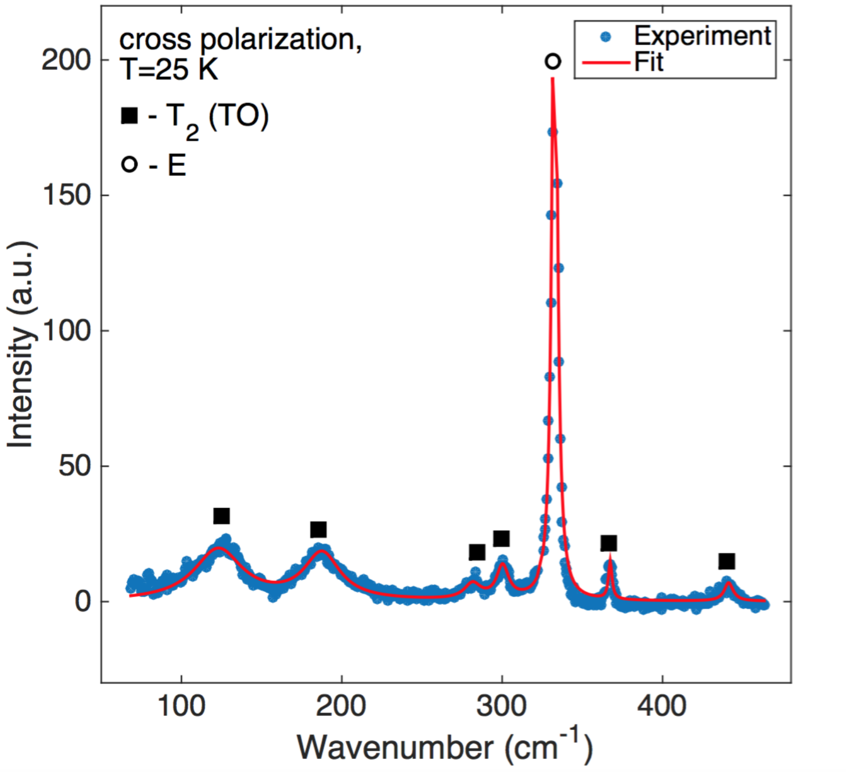

Figure 26: Raman spectrum at T=25 K (cross polarization configuration).

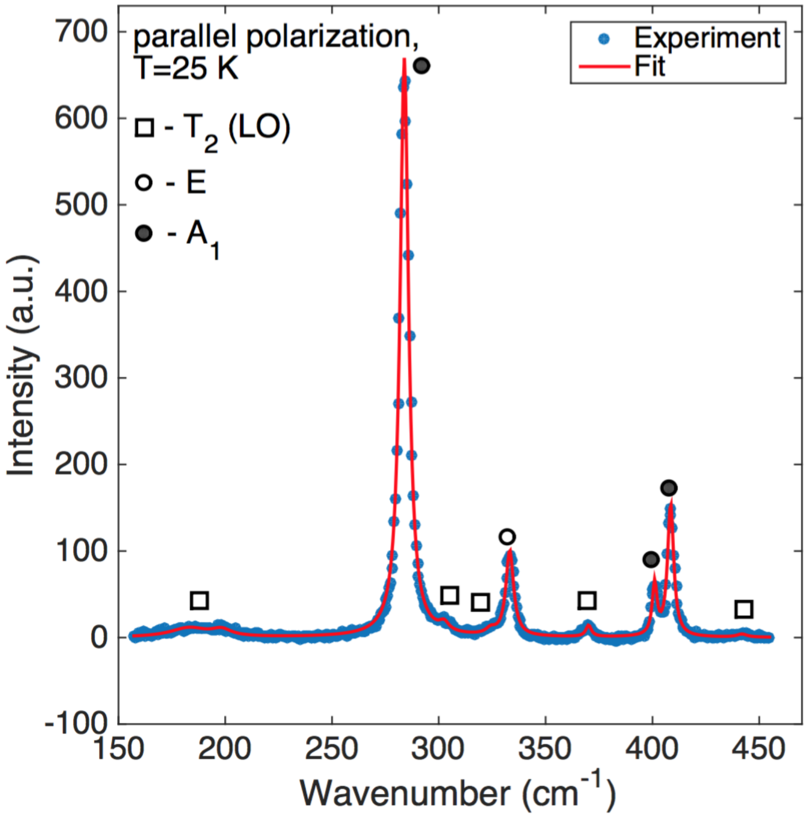

Figure 27: Raman spectrum at T=25 K (parallel polarization configuration).

Mode	T_2 (TO)				E	T_2 (TO)	
peak position (cm-1)	123	188	282	300	333	367	441

Table 8: Phonon modes of GaV_4S_8observed at 25 K for cross polarization configuration.

Mode	T_2 (LO)	A_1	T_2 (LO)		E	T_2 (LO)	A_1	A_1	T_2 (LO)
Peak position (cm-1)	183	284	303	324	333	370	401	409	442

Table 9: Phonon modes of GaV_4S_8observed at 25 K for parallel polarization configuration.

In the literature, the peaks at 126 cm-1 and 188 cm-1 (cross polarization, T=61 K) are assigned to be the Jahn-Teller active modes. This was concluded from these peaks being broad due to strong-electron phonon coupling. The two main factors, determining the phonon linewidth are the interaction with the other phonons (anharmonic terms) and the interaction with the electrons (electron-phonon coupling), which depends on the carrier density. During the JT structural transition, the atoms are displaced from their equilibrium positions which are described in terms of phonons. Interaction of electrons with these these displacements leads to the electron-phonon coupling. Since the Jahn-Teller distortion is strongly correlated with the electron-phonon coupling, the broadness of these peaks insinuate their JT activity. Moreover, these are the only peaks whose position is changed from higher to lower wavenumbers with temperature: all other peaks have an opposite behavior. However, this reasoning is not supported by any observable splitting of these modes after the transition to the ferroelectric phase. The splitting probably is not observed because the symmetry change is very weak or the peaks are too broad. Since the Raman spectra did not provide the explicit evidence of GaV_4S_8 undergoing the JT driven ferroelectric transition, the next step was to conduct time-resolved differential reflectivity measurements, which are discussed in the next subsection.

5.1.2 Differential reflectivity measurements for GaV_4S_8

Since the spontaneous Raman measurements did not provide conclusive results, we conducted differential reflectivity measurements in order to see the changes near the Jahn-Teller transition temperature $T_{JT} \backsimeq 42$ K. For this measurement the double-modulation pump-probe technique was used. The measurements were conducted in the temperature range from 20 to 55 K with 2.5-5 K steps for the (001) sample (Figure 28). The data was analyzed using a combination of fast Fourier transformation (FFT) and the Linear Prediction (LPM). The limitation of the FFT is related to poor resolution and spectral leakage, particularly with short delay scans. LPM is based on the singular value decomposition. This method was chosen because it provides an ability to accurately reconstruct of time-domain signal as a sum of decaying sinusoids with no a priori assumption on the number of terms. It often yields more accurate estimates of the oscillator frequencies than FFTs.

The raw signal measurement at T=55 K (which corresponds to the paraelectric phase of GaV_4S_8) is shown in the Figure 29. It can be seen that the reflectivity decreases and then slowly recovers. Pronounced oscillations are also seen, which are due to the excitation of coherent phonon modes. Before discussing the oscillations, the exponential background was subtracted. The fit is given in Figure 30.

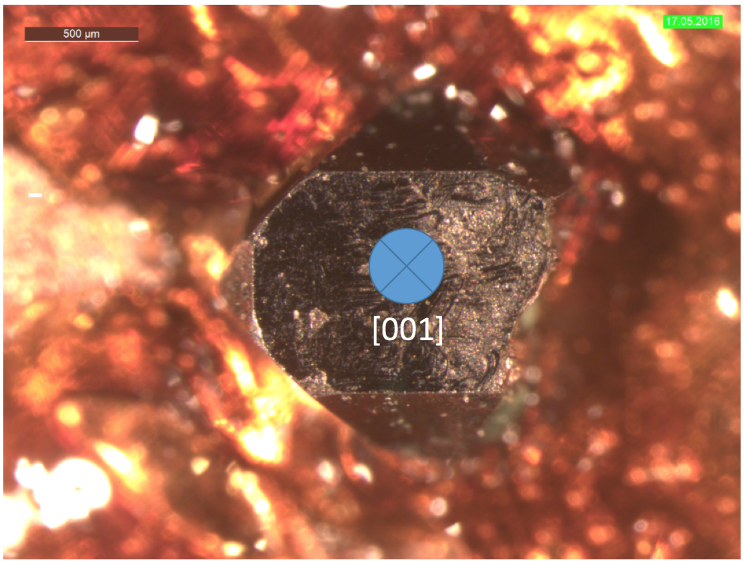

Figure 28: The (001) GaV_4S_8 sample.

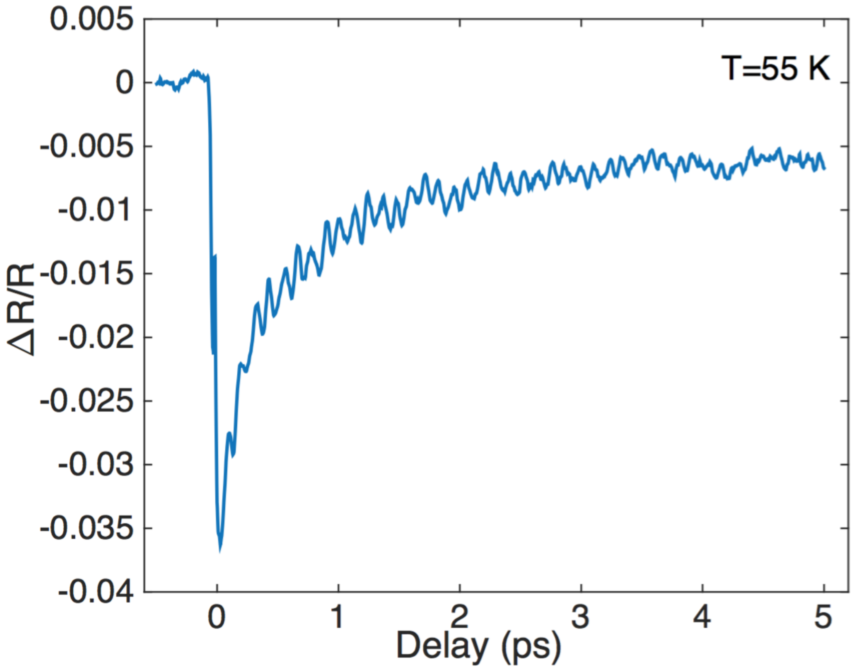

Figure 29: Reflectivity as the function of delay (T=55 K).

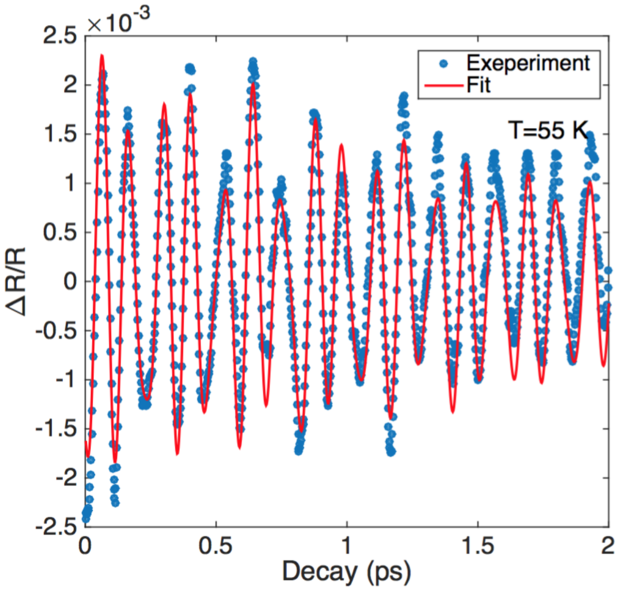

Figure 30: The fitted reflectivity oscillations (T=55 K).

Next, the windowed FFT of the signal was taken. Windowing can be used to minimize the spectral leakage at the cost of resolution. It is accomplished by multiplying the signal in the time domain by a window function. The one used here was periodic Hamming window function, which substantially lowers the level of the side lobes in FFT. Implementing windowing helps to better distinguish the peaks in the FFT, especially for the peaks with lower amplitudes. The windowed FFT of the time-domain signal is shown in the Figure 31. In the FFT, three peaks appear: at 286, 401, and 412 wavenumbers. These values are consistent with the ones obtained using LPM: the parameters for these modes are given in the tables 10 and 11 for the paraelectric and ferroelectric phases, respectively.

Since the driving mechanism behind the generation of coherent phonons is impulsive stimulated Raman scattering (ISRS) [61], the corresponding selection rule is given by

$$\frac{\Delta R}{R} \propto \left| \boldsymbol{e}_{pump} \cdot \overset{\leftrightarrow}{R} \cdot \boldsymbol{e}_{pump} \right| \left| \boldsymbol{e}_{probe} \cdot \overset{\leftrightarrow}{R} \cdot \boldsymbol{e}_{probe} \right|, \tag{5.14}$$

where, $\boldsymbol{e}_{pump}$ is the polarization vector of the pump beam, $\boldsymbol{e}_{probe}$ is the polarization vector of the probe beam, and R is the Raman tensor. The tensors were rotated to the basis:

$$x' = \frac{1}{\sqrt{2}}[110],$$

$$y' = \frac{1}{\sqrt{2}}[-110], \tag{5.15}$$

$$z' = [001].$$

The rotation matrix was deduced using the same approach as in the case of spontaneous Raman measurements. The resulting rotated tensors are given in the Appendix A.3. Table 12 gives the selection rules, calculated using the equation (5.14).

After comparing the position of the peaks in the FFT and the values obtained via LPM analysis with the Raman spectra (our measurements and literature), the observed phonon modes were determined to be A_1 modes. These were the only modes appearing well above the noise spectrum for both paraelectric and ferroelectric phases. While the A_1 mode is allowed for both T_d and C_{3v} symmetries, the other modes allowed by the selection rules were not seen. This is an unexpected result and could be possibly explained by the missing T_2(LO) and E modes being considerably weaker than A_1 mode and below our minimum sensitivity ($\Delta R/R \sim 10^{-4}$).

LPM predicted additional modes at lower wavenumbers which were not given in the table due to having quite different values in comparison with modes observed in the spontaneous Raman measurements. For T=55 K, two of these modes were at 103 cm^{-1} and 160 cm^{-1}. These modes could possibly be linked to the T_2(LO) phonons. As discussed in the Raman subsection, low frequency T_2 modes are most likely related to the JT transition. The peaks were broad, which indicates the dominance of the electron-phonon coupling term contribution to the phonon linewidth. The 103 cm^{-1} and 160 cm^{-1}modes obtained from the LPM analysis could be LO phonon-optical plasmon coupled modes. It was mentioned before that in the polar materials the LO phonons carry a macroscopic longitudinal electric field originating from the displacements of planes of positively and negatively charged atoms. The optical plasmons also carry a longitudinal electric field. When the plasmon frequency approaches the phonon frequency at sufficiently high carrier densities, it can couple to the phonon through their respective fields. This coupling results in the appearance of two repulsive phonon-plasmon coupled modes L_+ (higher frequency) and L_- (lower frequency),whose frequencies are strongly density dependent, with the L_- mode's frequency approaching the TO frequency at large densities. In contrast, the L_+ mode has a parabolic dispersion with respect to the carrier density n, starting at the LO frequency at $n = 0$. Hence, for intermediate carrier densities, the L_+ mode frequency will be above our detection limit, while the L_- would have lower values than expected in the absence of the plasmon coupling. Nevertheless, it is unclear why the other T_2 modes and the E modes do not appear in our measurements. The modes do not exhibit any pronounced change with temperature which could be due to the relative weakness of the rhombohedral distortion [52].

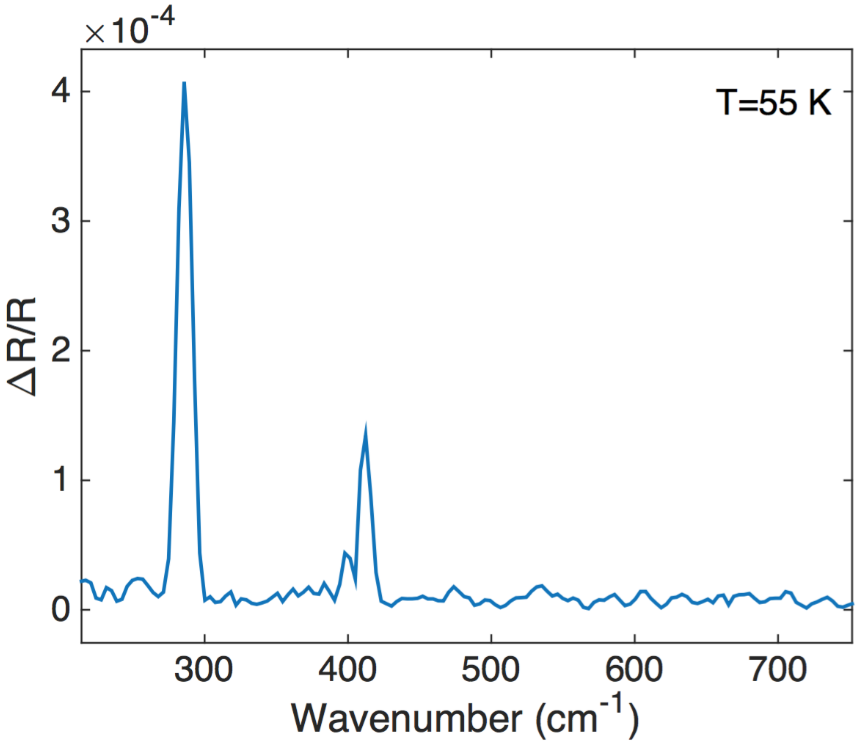

Figure 31: Fourier transform of the signal (T=55 K).

Wavenumber (cm^{-1})	Frequency (THz)	Decay rate (ps^{-1})	Phase	Amplitude
286	8.6	3.0	3.1	$4.0 \cdot 10^{-4}$
403	12.1	15.4	1.1	$4 \cdot 10^{-5}$
411	12.3	3.7	1.0	$1.5 \cdot 10^{-4}$

Table 10: Parameters of the fitted oscillators (T_d symmetry, T=55 K).

Wavenumber (cm^{-1})	Frequency (THz)	Decay rate (ps^{-1})	Phase	Amplitude
286	8.6	3.2	1.37	$3.3 \cdot 10^{-4}$
403	12.1	1.7	-1.2	$3.1 \cdot 10^{-5}$
411	12.3	7.1	-1.2	$1.4 \cdot 10^{-4}$

Table 11: Parameters of the fitted oscillators (C_{3v} symmetry, T=25 K).

Allowed modes	
T_d (paraelectric phase)	C_{3v} (ferroelectric phase)
A_1,$E(1)$,$T_2(z)$	$A_1(z)$,$E(x)$

Table 12: Selection rules for the reflectivity measurement.

Another interesting observation was the sign reversal of the pump-induced change in the reflectivity (Figure 32). The temperature dependence of the reflectivity extrema is given in Figure 33. This behavior can be caused by the structure changes in the region close to T_{JT} due to existence of the multiple domains in GaV_4S_8. Previously, it was shown that for multi-domain perovskite structures, the lattice parameters undergo splitting at the phase transition related to the Jahn-Teller distortion. This splitting is observed because the material has several domains and it leads to the change in volume of the crystal. M. Guennou *et al.* showed the dependence of the phonon mode frequencies with the change in the volume for $BiMnO_3$[62]. Since the lattice constants go back to their initial behavior after passing the region of interest, the volume changes only exists in the small window around the distortion parameter. Hence, the modes' frequencies go back to their behavior before the phase transition too. Such change in volume may occur in GaV_4S_8, causing the reflectivity sign to flip in the region around T_{JT}.

Lastly, Figure 34 shows the temperature dependence of the 286 cm^{-1} peak amplitude. It can be seen that it significantly changes when the temperature approaches the T_{JT} value, which is consistent with the distortion. However, it should be noted that since it is a fully symmetric mode, it cannot be the JT phonon.

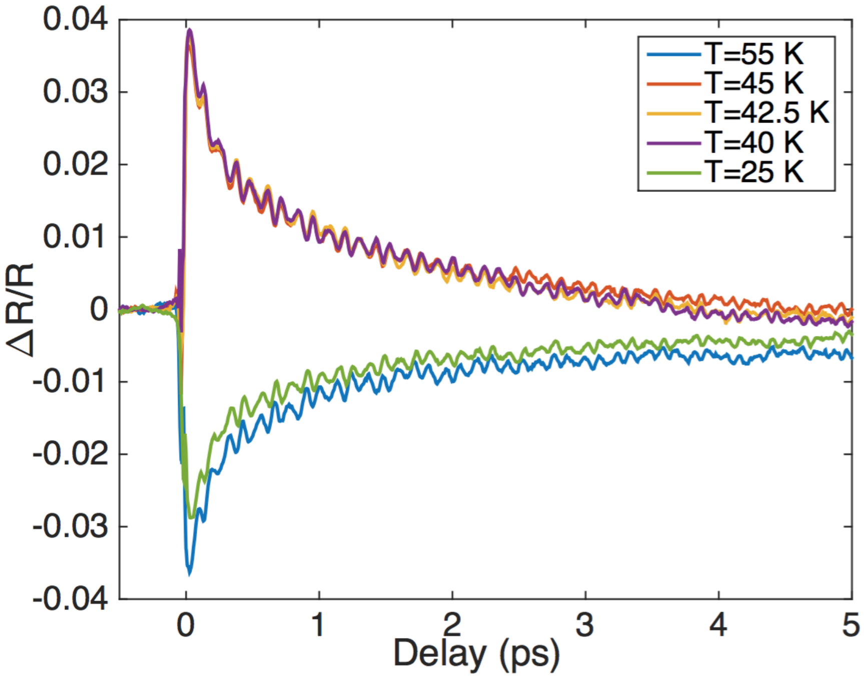

Figure 32: Comparison of the reflectivities for different temperatures.

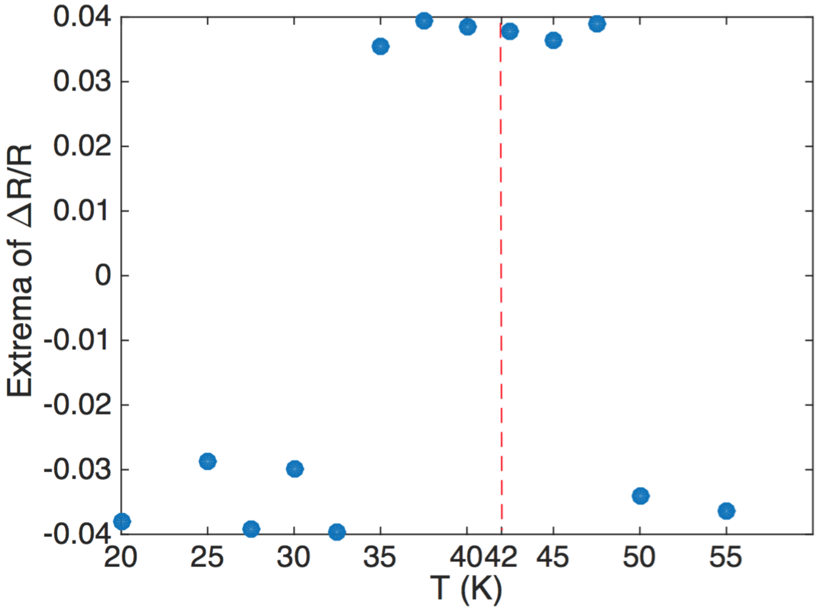

Figure 33: Extrema of reflectivities as the function of temperature.

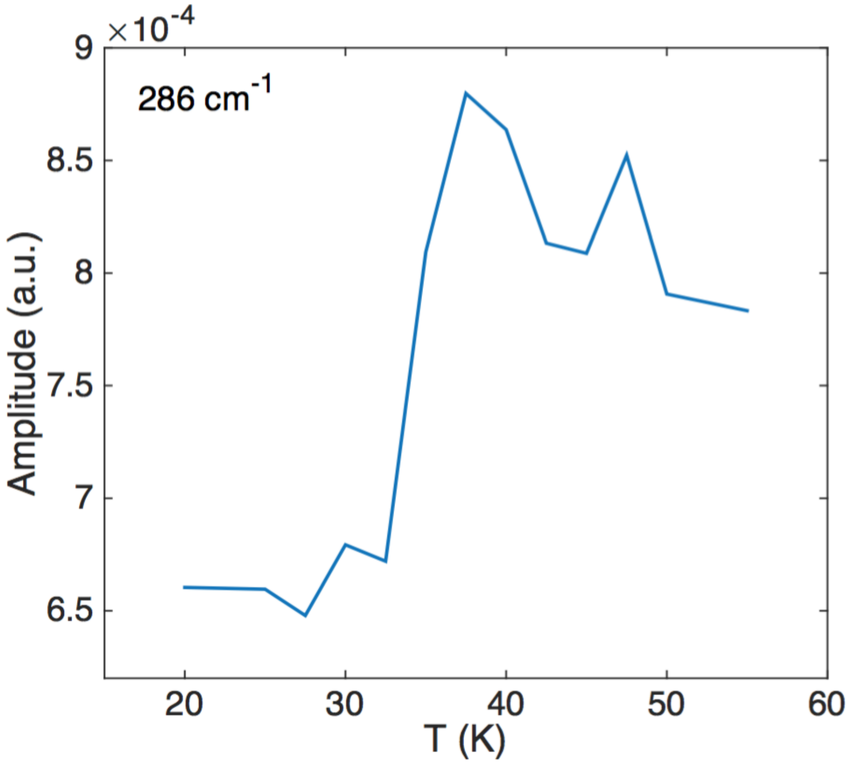

Figure 34: The change of the amplitude of 286.6 cm^{-1}peak with temperature.

5.2 Magnetization dynamics of GaV_4S_8

Time-resolved magneto-optical Kerr measurements for (111) GaV_4S_8 sample (Figure 22) were conducted using the double-modulation technique described in section 4.3. The probe beam was chopped at 787 Hz, and the pump beam was chopped with the PEM at 100 kHz (quarter-wave retardation). The sample in the magnetic cryostat was cooled down below the Néel temperature $T_c = 13$ K. As can be seen from Figure 16c, staying in the temperature region between 10 and 12 K, one can observe the magnetization spin dynamics in cycloidal and skyrmion magnetic phases by sweeping the magnetic field from 20 to 120 mT. The pump-induced Kerr rotation dependence on delay for the temperatures 10,11, and 12 K with varying magnetic field is given in Figure 35.

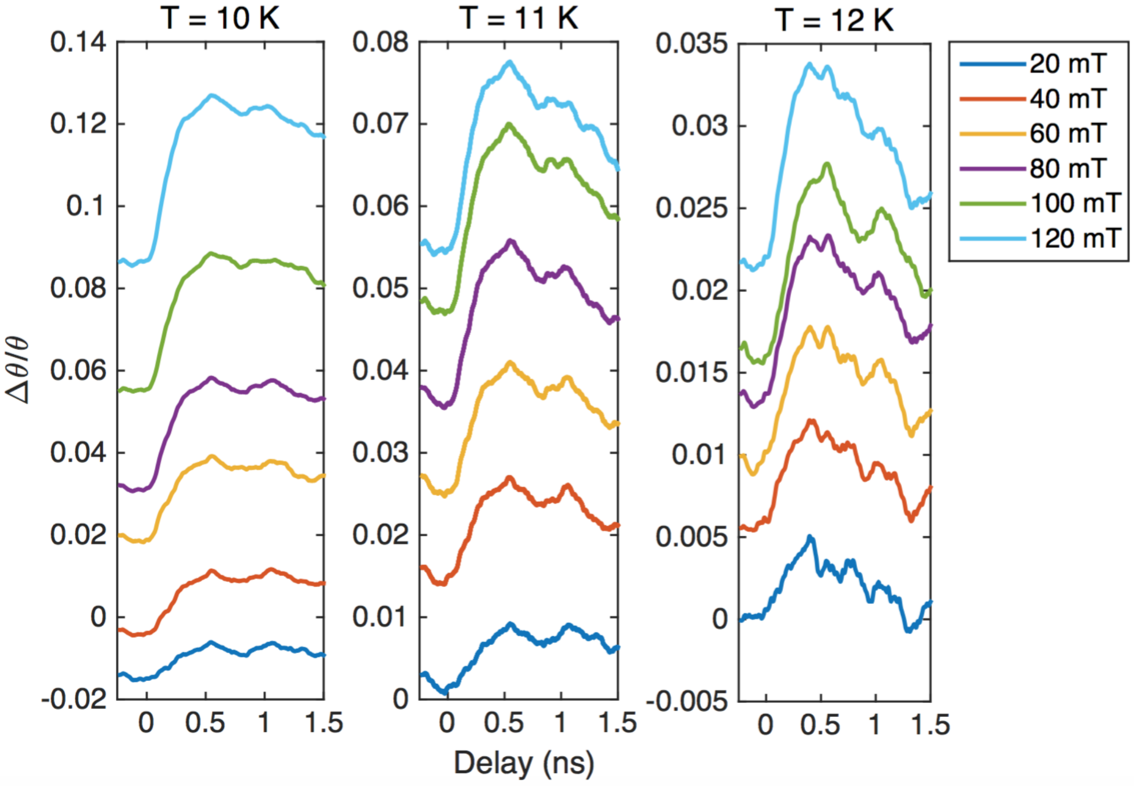

Figure 35: Kerr rotation as a function of delay at different temperatures and magnetic fields.

It can be seen that all the curves have a dip at approximately 0.75 ns which is most likely an artifact caused by the mechanical instabilities in the system. However, the Kerr rotation visibly changes and picks up some structure with varying magnetic field, especially at T=11 K and T=12 K. Hence, the next step was to selectively analyze a few features using LPM in order to see wether we observed magnetization spin dynamics which can be linked to one of the two possible magnetic phases in this region. The chosen features were corresponding to T=11 K, B=40 mT and T=12 K, B=100 mT with frequencies 5.2 GHz and 3.9 GHz, respectively. For the case of the feature T=11 K, B=40 mT, we are very close to the boundary between the skyrmion and cycloidal phases. If compared to Figure 36, the corresponding frequency indicates that it is the cycloidal excitation. The feature T=12 K, B=100 mT corresponds to the skyrmion phase.

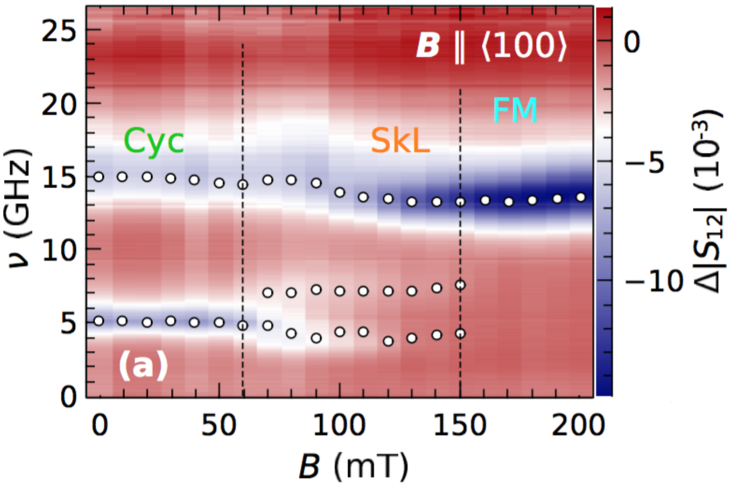

Figure 36: Color-coded plot of the transmission spectra in the frequency vs. magnetic field plane for T = 11 K [63].

Ethlers *et al.* observed two separated modes at 5 and 15 GHz in the cycloidal phase [63]. Such a splitting at low values of B arises from a competition between the DM interaction and the crystal field. However, we observe only the lower frequency mode in the cycloidal phase. As can be seen from Figure (35),there are only two periods of the oscillations in the measured time interval. Thus, a double pass method must be used in order to properly extract the oscillation frequencies. When increasing the magnetic field to 100 mT, we cross the phase boundary to the skyrmion phase and observe a Kerr rotation oscillation corresponding to one of the skyrmion modes. In the Figure 36a it can be seen that the low frequency mode at 5 GHz splits into two modes after the phase boundary is crossed, with the lower frequency mode (approx. 4 GHz) ascribed to a breathing mode and the higher frequency mode (approx. 7 GHz) to a CCW mode. In our measurement for the magnetic field B=100 mT at T=12 K, the frequency was determined to be 3.9 GHz, which is very close to the expected breathing mode frequency. However, we did not observe the CCW mode. Increasing the magnetic field to the values above 150 mT should allow for probing ferromagnetic phase. We did not measure above 120 mT, but the next step will be two measure in all magnetic phases existing for GaV_4S_8 at low temperatures. Moreover, the (111) sample, having two skyrmion and two cycloidal phases due to domain structure of the material, will be the focus of the future experiments.

5.3 Magnetezation dynamics of Cu_2OSeO_3

The magnetization dynamics of Cu_2OSeO_3 were studied using the double-modulation technique proposed by Koopmas [64]. The measurements were conducted in a polar MOKE geometry. The Ti:Sapphire oscillator was cavity dumped at 2MHz delivering on a sample fluence of 40 nJ/pulse. The pump pulse was right circularly polarized and th polarization of the probe was modulated by PEM at 50 kHz. The probe beam was then detected after passing through an analyzer. The sample was cooled down to 57.7 K, which corresponds to the Skyrmion Phase. The magnetic field B was applied perpendicular to the sample surface and its value was varied from 80 to 140 mT.

Figure 37 demonstrates the dependance of the Kerr rotation on the time delay. The obtained raw data for different magnetic field values was first smoothed using a moving average and then fit with a sine wave. Theoretical studies claim that spin dynamics in the skyrmion phase depend on the magnetic filed orientation.: for an in-plane field the CW and CCW rotational modes should be observed and for an out-of-plane field-the breathing mode should be the only accessible mode [40]. Due to our geometry we expect to see only the breathing mode.

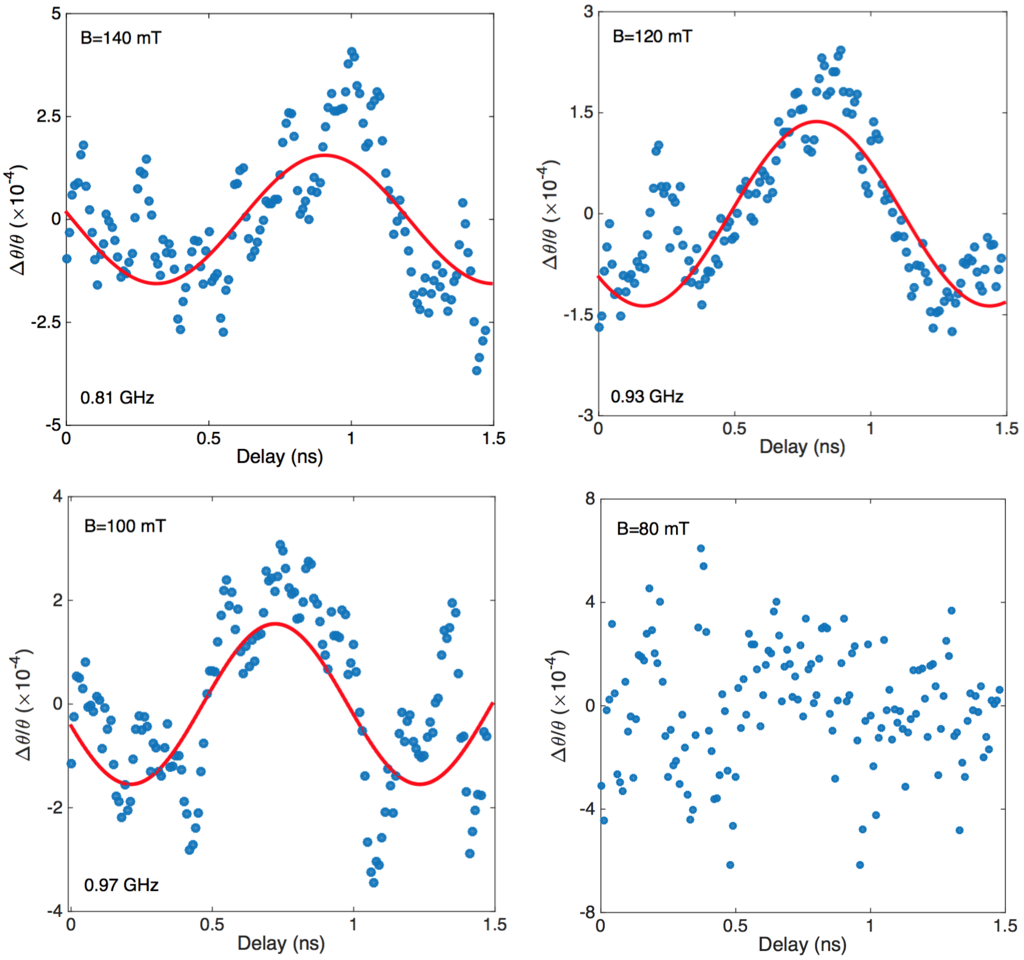

Figure 37: Kerr rotation as a function of delay.

The oscillations are present for values of applied field B in the range of 100-140 mT and disappear at 80 mT (B values and corresponding frequencies f are given in table 13). The corresponding frequencies of the breathing mode for each field are in the GHz range and decrease with higher magnetic field values (Figure 38).These results are consistent with the previous studies by N. Ogawa *et al.*, where the magnetization dynamics were induced by the inverse Faraday effect [25]. However, the frequencies are lower (1.7 GHz from the inverse Faraday measurement). This could be caused by the deviation from the T=57. If the real sample temperature is on the edge of the skyrmion phase, the mode frequency diminishes [25] . The values of applied magnetic field in our case is higher than the ones reported by R. Ogawa (20 mT) and R. Versteeg [36] (magnetic field varying from 20 to 50 mT for the skyrmion phase) and this is currently not well understood.

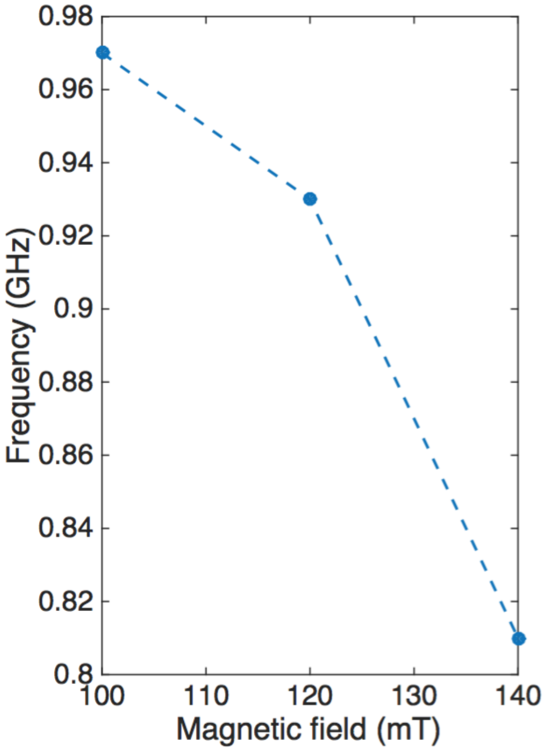

Figure 38: Oscillation frequency as a function of applied magnetic field.

B (mT)	f (GHz)
140	0.81
120	0.93
100	0.97
80	-

Table 13: Applied magnetic field values B and corresponding frequencies f.

6 Conclusions and outlook

During the course of this work, properties of skyrmion materials were probed with different techniques. While the main goal was to observe the magnetization dynamics using the TR-MOKE method, we also attempted to probe the coherent phonon modes of GaV_4S_8 which are involved in the Jahn-Teller distortion. Spontaneous Raman spectra for different polarization configurations were measured for the temperature range around the transition temperature T_{JT}. Surprisingly, no splitting of the modes was observed, as was expected from group theory. However, some of the observed phonon peaks showed behavior which might indicate that they are JT-active. This can be due to the weakness of the JT effect: the change in structure is so small that T_2 peaks are dwarfed by the stronger A_1 and E modes.

Since the spontaneous Raman measurements did not provide conclusive results, we then conducted differential reflectivity measurement using the double modulation pump-probe technique. The results of this experiment also did not show any evidence of mode splitting due to a change in symmetry. Nevertheless, we observed a sign change of the pump-induced reflectivity. This behavior could originate from the multi-domain structure of GaV_4S_8, which leads to change in the volume of the crystal during the structural transition. This change of reflectivity sign gives evidence that the material actually undergoes the structural phase transition. Combining these observations with the Raman results, it can be concluded that the reason why we did not observe the splitting or shifts of the modes when going from higher to lower symmetry is that these JT-active T_2 (LO) (only longitudinal T_2 phonons were allowed by selection rules in case of reflectivity measurement) are actually very weak in comparison to the other modes.Thus, we have to try something else in order to try see the change predicted by the group theory. For instance, we can try to use the reflective electro-optic sampling (REOS) technique, which allows to probe T_2(LO) modes selectively.

Next, the skyrmion dynamics GaV_4S_8 of and Cu_2OSeO_3were studied. Observed spin dynamics were consistent with the results reported in literature, but for Cu_2OSeO_3, the signal-to-noise ratio was too low to determine the oscillation frequencies accurately. Additionally, we could not observe all possible modes because there were only a few oscillatory periods over the measured time. In order to increase the this interval, we need to extend our measurement range using a double pass configuration. Moreover, when the magnetization dynamics was measured, the experimental setup proposed by Koopmans was originally utilized.This technique suffered from an overall high noise level. In the future, TR-MOKE measurements for Cu_2OSeO_3will be made using the polarization bridge for detection. However, mostly we are interested in continuing experiments on GaV_4S_8, since the selection rules are not established for this material, in contrast to Cu_2OSeO_3.So far, we have seen that we observe the breathing mode for out of plane magnetic field, which coincides with what we expect for Cu_2OSeO_3at the same conditions. Still, we have to conduct measurements in all possible configurations to draw any conclusions about the selection rules.

A Appendix

A.1 Derivation of expression for Voigt vector as a function of dielectric tensor elements

Complex refractive index is given by

$$n_\pm = \sqrt{\varepsilon_{xx} \pm i\varepsilon_{xy}}. \tag{6.1}$$

Complex reflection coefficient can be expressed as

$$\rho_\pm = r_\pm e^{i\theta_\pm} = \frac{n_\pm - 1}{n_\pm + 1}, \tag{6.2}$$

where $\theta_\pm$ is the phase difference between incident and reflected light.

The ration of reflection coefficients of right circularly (RCP) and left circularly (LCP) polarized light yields

$$\frac{\rho_+}{\rho_-} = \frac{r_+}{r_-} e^{i(\theta_+ - \theta_-)} = e^{-2i\theta_k} \frac{1+\eta_k}{1-\eta_k}, \tag{6.3}$$

where Kerr rotation and ellipticity are given by

$$\theta_k = -\frac{1}{2}(\theta_+ - \theta_-), \eta_k = \frac{r_+ - r_-}{r_+ + r_-}. \tag{6.4}$$

Expanding (6.3) for small θ_k and η_k, we get

$$\frac{\rho_+}{\rho_-} \approx (1 - 2i\theta_k)(1 + 2\eta_k) \approx 1 - 2i\theta_k + 2\eta_k. \tag{6.5}$$

Considering the ratio between the reflected electric fields for RCP and LCP light , we have

$$\frac{E_{ref,+}}{E_{ref,-}} = \frac{E_{in,+} \cdot \rho_+}{E_{in,-} \cdot \rho_-} = \frac{\rho_+}{\rho_-}, \tag{6.6}$$

where$E_{in,\pm}$is the electric field of incident light.

If we plug (6.1) and (6.2) into (6.6), we will have

$$\frac{\rho_+}{\rho_-} = \frac{\left(\sqrt{\varepsilon_{xx} + i\varepsilon_{xy}} - 1\right)\left(\sqrt{\varepsilon_{xx} - i\varepsilon_{xy}} + 1\right)}{\left(\sqrt{\varepsilon_{xx} + i\varepsilon_{xy}} + 1\right)\left(\sqrt{\varepsilon_{xx} - i\varepsilon_{xy}} - 1\right)}. \tag{6.7}$$

Expanding (6.7) for small ε_{xy}, using $\sqrt{1+x} \approx 1 + \frac{x}{2}$,we get

$$\frac{\rho_+}{\rho_-} = \frac{2i\varepsilon_{xy}}{\sqrt{\varepsilon_{xx}}(\varepsilon_{xx} - 1)} + 1. \tag{6.8}$$

Comparing (6.5) and (6.8) gives expression for the Voigt vector:

$$\tilde{\Theta}_{\mathrm{k}} = \theta_k + i\eta_k = \frac{-\varepsilon_{xy}}{\sqrt{\varepsilon_{xx}}(\varepsilon_{xx} - 1)}. \tag{6.9}$$

A.2. Rotation of the Raman tensors for a (111) sample

Raman tensors in cartesian basis for the T_d symmetry are given by

$$R(A_1) = \begin{pmatrix} a & 0 & 0 \\ 0 & a & 0 \\ 0 & 0 & a \end{pmatrix}, R(E(1)) = \begin{pmatrix} b & 0 & 0 \\ 0 & b & 0 \\ 0 & 0 & -2b \end{pmatrix},$$

$$R(E(2)) = \begin{pmatrix} -\sqrt{3b} & 0 & 0 \\ 0 & \sqrt{3b} & 0 \\ 0 & 0 & 0 \end{pmatrix}, \tag{6.10}$$

$$R(T_2(x)) = \begin{pmatrix} 0 & 0 & 0 \\ 0 & 0 & d \\ 0 & d & 0 \end{pmatrix}, R(T_2(y)) = \begin{pmatrix} 0 & 0 & d \\ 0 & 0 & 0 \\ d & 0 & 0 \end{pmatrix}, R(T_2(z)) = \begin{pmatrix} 0 & d & 0 \\ d & 0 & 0 \\ 0 & 0 & 0 \end{pmatrix}.$$

Raman tensors for the C_{3v} symmetry are

$$R(A_1(z)) = \begin{pmatrix} a & 0 & 0 \\ 0 & a & 0 \\ 0 & 0 & b \end{pmatrix}, R(E(x)) = \begin{pmatrix} 0 & c & d \\ c & 0 & 0 \\ d & 0 & 0 \end{pmatrix}, \tag{6.11}$$

$$R(E(y)) = \begin{pmatrix} c & 0 & 0 \\ 0 & -c & d \\ 0 & d & 0 \end{pmatrix}.$$

In order to rotate these tensors, one can construct the direction cosine matrix (DCM) which gives the Euler angles. The DCM is given by

$$DCM = \begin{pmatrix} Xx & Xy & Xz \\ Yx & Yy & Yz \\ Zx & Zy & Zz \end{pmatrix}, \tag{6.12}$$

where X, Y, Z gives a new basis and x, y, z gives a cartesian basis. The Euler angles are then be calculated as

$$\varphi = arctan\left(\frac{Xy}{Xx}\right), \theta = -arcsin(Xz), \psi = arctan\left(\frac{Zy}{Zz}\right), \tag{6.13}$$

where the angles φ, θ, ψ correspond to the axis x, y, z, respectively.

The matrices for rotation around x, y, and z are given by

$$M_x = \begin{pmatrix} 0 & 0 & 0 \\ 0 & cos\varphi & -sin\varphi \\ 0 & sin\varphi & cos\varphi \end{pmatrix}, M_y = \begin{pmatrix} cos\theta & 0 & -sin\theta \\ 0 & 0 & 0 \\ sin\theta & 0 & cos\theta \end{pmatrix}, \tag{6.14}$$

$$M_z = \begin{pmatrix} cos\psi & -sin\psi & 0 \\ sin\psi & cos\psi & 0 \\ 0 & 0 & 1 \end{pmatrix}.$$

Rotation matrix is then calculated as

$$M = M_z M_y M_x. \tag{6.15}$$

The resulting rotation matrix yields:

$$M = \begin{pmatrix} \frac{1}{\sqrt{2}} & \frac{1}{\sqrt{6}} & \frac{1}{\sqrt{3}} \\ -\frac{1}{\sqrt{2}} & \frac{1}{\sqrt{6}} & \frac{1}{\sqrt{3}} \\ 0 & -\frac{\sqrt{2}}{\sqrt{3}} & \frac{1}{\sqrt{3}} \end{pmatrix}. \tag{6.16}$$

Finally, one can calculate the rotated Raman tensors using

$$\overleftrightarrow{R}_{new} = M^T \overleftrightarrow{R} M. \tag{6.17}$$

A.3. Rotation of the Raman tensors for a (001) sample

Rotation matrix is calculated as described in A.2. The result yields:

$$M = \begin{pmatrix} \frac{1}{\sqrt{2}} & -\frac{1}{\sqrt{2}} & 0 \\ \frac{1}{\sqrt{2}} & \frac{1}{\sqrt{2}} & 0 \\ 0 & 0 & 1 \end{pmatrix}.$$

Rotated Raman tensors for the T_d symmetry are given by:

$$R(A_1) = \begin{pmatrix} a & 0 & 0 \\ 0 & a & 0 \\ 0 & 0 & a \end{pmatrix}, R(E(1)) = \begin{pmatrix} b & 0 & 0 \\ 0 & b & 0 \\ 0 & 0 & -2b \end{pmatrix},$$

$$R(E(2)) = \begin{pmatrix} 0 & \sqrt{3}b & 0 \\ \sqrt{3}b & 0 & 0 \\ 0 & 0 & 0 \end{pmatrix}, \tag{6.18}$$

$$R(T_2(x)) = \begin{pmatrix} 0 & 0 & \frac{d}{\sqrt{2}} \\ 0 & 0 & \frac{d}{\sqrt{2}} \\ \frac{d}{\sqrt{2}} & \frac{d}{\sqrt{2}} & 0 \end{pmatrix}, R(T_2(y)) = \begin{pmatrix} 0 & 0 & \frac{d}{\sqrt{2}} \\ 0 & 0 & -\frac{d}{\sqrt{2}} \\ \frac{d}{\sqrt{2}} & -\frac{d}{\sqrt{2}} & 0 \end{pmatrix},$$

$$R(T_2(z)) = \begin{pmatrix} d & 0 & 0 \\ 0 & -d & 0 \\ 0 & 0 & 0 \end{pmatrix}.$$

Rotated Raman tensors for the C_{3v} symmetry are given by:

$$R(A_1(z)) = \begin{pmatrix} a & 0 & 0 \\ 0 & a & 0 \\ 0 & 0 & b \end{pmatrix}, R(E(x)) = \begin{pmatrix} c & 0 & \frac{d}{\sqrt{2}} \\ 0 & -c & -\frac{d}{\sqrt{2}} \\ \frac{d}{\sqrt{2}} & -\frac{d}{\sqrt{2}} & 0 \end{pmatrix}, \tag{6.19}$$

$$R(E(y)) = \begin{pmatrix} 0 & -c & \frac{d}{\sqrt{2}} \\ -c & 0 & \frac{d}{\sqrt{2}} \\ \frac{d}{\sqrt{2}} & \frac{d}{\sqrt{2}} & 0 \end{pmatrix}.$$

B Acknowledgements

I would like to thank Prof. van Loosdrecht for the supervision of my thesis and his valuable advice during the whole working process. I am also very grateful for the help of Dr. Prashant Padmanabhan and Rolf Versteeg, with whom I worked most of my time in the group. It was a great learning experience and it was a pleasure to spend a year working with these people. Finally, I want to thank my friends and family who were very supporting and put up with my mood swings during the writing of this thesis. They always encouraged me to continue my research in spite of any difficulties occurring on my way.

List of Figures

List of Tables

References

[1] Skyrme, T. H. R. A Non-Linear Field Theory. *Proceedings of the Royal Society A: Mathematical, Physical and Engineering Sciences* **260**, 127–138 (1961).

[2] Mühlbauer, S. Skyrmion lattice in a chiral magnet. *Science* **323**, 915–919 (2009).

[3] Bogdanov, A. & Yablonskii, D. Thermodynamically stable "vortices" in magnetically ordered crystals. The mixed state of magnets. *Zh. Eksp. Teor. Fiz* **95**, 178 (1989).

[4] Bogdanov, A. & Hubert, A. Thermodynamically stable magnetic vortex states in magnetic crystals. *Journal of Magnetism and Magnetic Materials* **138**, 255–269 (1994).

[5] Rössler, U. K., Bogdanov, A. N. & Pfleiderer, C. Spontaneous skyrmion ground states in magnetic metals. *Nature* **442**, 797–801 (2006).

[6] Binz, B., Vishwanath, A. & Aji, V. Theory of the helical spin crystal: A candidate for the partially ordered state of MnSi. *Physical Review Letters* **96**, 1–4 (2006).

[7] Tewari, S., Belitz, D. & Kirkpatrick, T. R. Blue quantum fog: Chiral condensation in quantum helimagnets. *Physical Review Letters* **96**, 1–4 (2006).

[8] Felser, C. Skyrmions. *Angewandte Chemie - International Edition* **52**, 1631–1634 (2013).

[9] Malozemoff, A. P. & Slonczewski, J. C. *Magnetic Domain Walls in Bubble Materials* (Academic Press, New York, 1979).

[10] Bader, S. D. Colloquium: Opportunities in nanomagnetism. *Reviews of Modern Physics* **78** (2006).

[11] Nagaosa, N. & Tokura, Y. Topological properties and dynamics of magnetic skyrmions. *Nature nanotechnology* **8**, 899–911 (2013).

[12] Jonietz, F. *et al.* Spin Transfer Torques in MnSi at Ultralow Current Densities. *Science* **330**, 1648–1651 (2010).

[13] Zutić, I. & Dery, H. Spintronics: Taming spin currents. *Nature materials* **10**, 647–648 (2011).

[14] Münzer, W. *et al.* Skyrmion lattice in the doped semiconductor $Fe_{1-x}Co_xSi$. *Physical Review B - Condensed Matter and Materials Physics* **81**, 1–4 (2010).

[15] Yu, X. Z. *et al.* Real-space observation of a two-dimensional skyrmion crystal. *Nature* **465**, 901–904 (2010).

[16] Yu, X. Z. *et al.* Near room-temperature formation of a skyrmion crystal in thin-films of the helimagnet FeGe. *Nature materials* **10**, 106–109 (2011).

[17] Seki, S., Yu, X. Z., Ishiwata, S. & Tokura, Y. Observation of Skyrmions in a Multiferroic Material. *Science* **336**, 198–201 (2012).

[18] Bogdanov, A. & Hubert, A. The properties of isolated magnetic vortices. *Physica Status Solidi (B)* **186**, 527–543 (1994).

[19] Kézsmárki, I. *et al.* Néel-type skyrmion lattice with confined orientation in the polar magnetic semiconductor GaV_4S_8. *Nature materials* **14**, 1116–22 (2015).

[20] Milde, P. *et al.* Unwinding of a skyrmion lattice by magnetic monopoles. *Science (New York, N.Y.)* **340**, 1076–80 (2013).

[21] Pfleiderer, C. Magnetic order: Surfaces get hairy. *Nature Physics* **7**, 673–674 (2011).

[22] Heinze, S. *et al.* Spontaneous atomic-scale magnetic skyrmion lattice in two dimensions. *Nature Physics* **7**, 713–718 (2011).

[23] Ogasawara, T., Iwata, N., Murakami, Y., Okamoto, H. & Tokura, Y. Submicron-scale spatial feature of ultrafast photoinduced magnetization reversal in TbFeCo thin film. *Applied Physics Letters* **94**, 94–97 (2009).

[24] Finazzi, M. *et al.* Laser-induced magnetic nanostructures with tunable topological properties. *Physical Review Letters* **110**, 1–5 (2013).

[25] Ogawa, N., Seki, S. & Tokura, Y. Ultrafast optical excitation of magnetic skyrmions. *Scientific reports* **5**, 9552 (2015).

[26] Seki, S. & Mochizuki, M. *Skyrmions in Magnetic Materials* (2016).

[27] Lin, Y. S., Grundy, P. J. & Giess, E. A. Bubble domains in magnetostatically coupled garnet films. *Applied Physics Letters* **23**, 485–487 (1973).

[28] Garel, T. & Doniach, S. Phase transitions with spontaneous modulation-the dipolar Ising ferromagnet. *Physical Review B* **26**, 325–329 (1982).

[29] Suzuki, T. A study of magnetization distribution of submicron bubbles in sputtered Ho-Co thin films. *Journal of Magnetism and Magnetic Materials* **31-34**, 1009–1010 (1983).

[30] Okubo, T., Chung, S. & Kawamura, H. Multiple-q states and the Skyrmion lattice of the triangular-lattice Heisenberg antiferromagnet under magnetic fields. *Physical Review Letters* **108**, 1–5 (2012).

[31] Dzyaloshinsky, I. A thermodynamic theory of "weak" ferromagnetism of antiferromagnetics. *Journal of Physics and Chemistry of Solids* **4**, 241–255 (1958).

[32] Moriya, T. Anisotropic superexchange interaction and weak ferromagnetism. *Physical Review* **120**, 91–98 (1960).

[33] Bak, P. & Jensen, M. H. Theory of helical magnetic structures and phase transitions in MnSi and FeGe. *Journal of Physics C: Solid State Physics* **13**, L881–L885 (1980).

[34] Everschor, K. *Current-induced dynamics of chiral magnetic structures.* Ph.D. thesis (2012).

[35] Yu, X. *et al.* Magnetic stripes and skyrmions with helicity reversals. *Proceedings of the National Academy of Sciences* **109**, 8856–8860 (2012).

[36] Versteeg, R. B. *et al.* Optically probing symmetry breaking in the chiral magnet Cu_2OSeO_3 1–9 (2016).

[37] Schütte, C. Skyrmions and Monopoles in Chiral Magnets & Correlated Heterostructures. *PhD Thesis* (2014).

[38] Adams, T. *et al.* Long-wavelength helimagnetic order and skyrmion lattice phase in Cu_2OSeO_3. *Physical Review Letters* **108**, 1–5 (2012).

[39] Okamura, Y. *et al.* Microwave magnetoelectric effect via skyrmion resonance modes in a helimagnetic multiferroic. *Nature Communications* **4**, 2391 (2013).

[40] Mochizuki, M. Spin-wave modes and their intense excitation effects in Skyrmion crystals. *Physical Review Letters* **108**, 1–5 (2012).

[41] H. Effenberger and F. Pertlik. Die Kristallstrukturen der Kupfer(II)-oxoselenite Cu_2OSeO_3 (kubisch und monoklin) und $Cu_4O(SeO_3)_3$ (monoklin und triklin). *Monatshefte für Chemie* **117**, 887 (1986).

[42] Tucker, G. S., White, J. S., Romhányi, J. & Szaller, D. Spin excitations in the skyrmion host Cu_2OSeO_3. *Physical Review B* **93**, 054401 (2016).

[43] Bichler, D. & Johrendt, D. Interplay of magnetism and bonding in $GaV_{4-x}Cr_xSe_8$. *Chemistry of Materials* **23**, 3014–3019 (2011).

[44] Nakamura, H. *et al.* Low-field multi-step magnetization of GaV_4S_8 single crystal. *Journal of Physics: Conference Series* **145**, 012077 (2009).

[45] Pocha, R., Johrendt, D., Haus, D. & Mu, D. Electronic and Structural Instabilities in GaV_4S_8 and $GaMo_4S_8$. *Structure* 2882–2887 (2000).

[46] Gürs, K. & Müller, R. Breitband-modulation durch steuerung der emission eines optischen masers (Auskoppelmodulation). *Physics Letters* **5**, 179–181 (1963).

[47] Gürs, K. Beats and modulation in optical ruby lasers. In Grivet, P. & Bloembergen, N. (eds.) *Quantum Electronics III*, 1113–1119 (Columbia University Press, New York, 1964).

[48] Tang, C. & Statz, H. Zeeman effect and nonlinear interactions between oscillating laser modes. In Grivet, P. & Bloembergen, N. (eds.) *Quantum Electronics III*, 469–498 (Columbia University Press, New York, 1964).

[49] Sutter, D. H. *et al.* Semiconductor saturable-absorber mirror-assisted Kerr-lens mode-locked Ti: sapphire laser producing pulses in the two-cycle regime. *Optics Letters* **24**, 631–633 (1999).

[50] Prasankumar, R. P. & Taylor, A. J. *Optical techniques for solid-state materials characterization* (Crc Press, 2011).

[51] Oppeneer, P. Magneto-optical Kerr spectra. *Handbook of Magnetic Materials* 229–422 (2001).

[52] Hlinka, J. *et al.* Lattice modes and the Jahn-Teller ferroelectric transition of GaV_4S_8. *Physical Review B* **94**, 060104 (2016).

[53] Keimer, B. Ferroelectricity driven by orbital order. *Nature materials* **5**, 933 (2006).

[54] Barone, P., Yamauchi, K. & Picozzi, S. Ferroelectricity due to orbital ordering in E-type undoped rare-earth manganites. *Physical Review Letters* **106**, 1–4 (2011).

[55] Singh, K. *et al.* Orbital-Ordering-Driven Multiferroicity and Magnetoelectric Coupling in $\mathrm{GeV_4\ S_8}$. *Physical Review Letters* **113**, 137602 (2014).

[56] Wang, Z. *et al.* Polar Dynamics at the Jahn-Teller Transition in Ferroelectric $\mathrm{GaV_4S_8}$. *Physical Review Letters* **115**, 1–5 (2015).

[57] Raman, C. V. & Krishnan, K. S. A new type of secondary radiation. *Nature* **121**, 501–502 (1928).

[58] Mandelstam, L. & Landsberg, G. Eine neue Erscheinung bei der Lichtzerstreuung in Krystallen. *Naturwiss.* **16**, 557–558 (1928).

[59] Kuzmany, H. *Solid-State Spectroscopy: An Introduction* (Springer, 1998).

[60] Yu, P. Y. & Cordona, M. *Fundamentals of Semiconductors: Physics and Materials Properties* (Springer, 2010).

[61] Ishioka, K. & Misochko, O. V. Coherent Lattice Oscillations in Solids and Their Optical Control Part II. New Detection Techniques and Optical Control. *Springer Series in Chemical Physics* **98**, 47–63 (2010).

[62] Guennou, M. *et al.* Jahn-teller, polarity, and insulator-to-metal transition in BiMnO3 at high pressure. *Physical Review Letters* **112** (2014).

[63] Ehlers, D. *et al.* Magnetic Excitations in the Multiferroic Néel-type Skyrmion Host $\mathrm{GaV_4S_8}$ **1116**, 1–5 (2015).

[64] Kamel, B. H. *Spin Dynamics in Confined Magnetic Structures II* (2002).